Article

Understanding Landslide Expression in SAR Backscatter Data: A Global Study

Erin Lindsay [1]*, Alexandra Jarna Garnerød[2,3], Graziella Devoli[4], Johannes Reiche[5], Steinar Nordal[1], Regula Frauenfelder[6], Lars-Christian Tokle[7]

1* Department of Civil and Environmental Engineering, Norwegian University of Science and Technology, 7034 Trondheim, Norway; erin.lindsay@ntnu.no (E.L.); steinar.nordal@ntnu.no (S.N.)
2 Department of Geography, Norwegian University of Science and Technology, 7049 Trondheim, Norway; alexandra.jarna@ntnu.no (A.J.G.);
3 Geological Survey of Norway (NGU), 7040 Trondheim, Norway; alexandra.jarna@ngu.no
4 Norwegian Directorate of Energy and Water, Oslo, Norway. g.de@nve.no (G.D.)
5 Laboratory of Geo-Information Science and Remote Sensing, Wageningen University & Research, Droevendaalsesteeg 3, 6708 PB Wageningen, The Netherlands; johannes.reiche@wur.nl (J.R.);
6 Norwegian Geotechnical Institute (NGI), 0806 Oslo, Norway; regula.frauenfelder@ngi.no (R.F.);
7 Department of Mathematics and Cybernetics, Norwegian University of Science and Technology, 7034 Trondheim, Norway; lars-christian.n.tokle@ntnu.no (LT)
* Corresponding author: erin.lindsay@ntnu.no

Abstract: During disaster response, clouds or darkness can prevent the use of optical images for detecting consequences of natural disasters, including landslides. In these situations, radar images can be used to detect changes more rapidly. However, Synthetic Aperture Radar (SAR) backscatter intensity images are underutilized for landslide detection. Unfortunately, there remains a lack of understanding about how to interpret landslide signatures in SAR imagery. In this study, we investigate how the morphometric features and material properties of landslides, and preexisting land cover, control their expression in SAR backscatter intensity change images. Trends in the spatial and temporal signatures of over 1000 landslides in 30 diverse case studies are investigated, using multi-temporal composites and dense time-series of Sentinel-1 C-band SAR backscatter intensity data. The results show that the orientation of landslide surfaces relative to the sensor, pre-existing land cover, and the roughness of the landslide surface, determine whether landslides will produce an increase or decrease in backscatter intensity values. In certain cases, we can identify morphometric features of landslides (e.g. scarps, transit zone, deposits, ponding) and material properties. Generally, we see that landslides appear most clearly with a strong increase in intensity when they occur in herbaceous vegetation or non-vegetated ground surfaces, due to an increase in surface roughness. While in forested or densely vegetated areas, landslides produce a more complex signature with both decreases due to radar shadow and vegetation removal, and an adjacent edge of increased intensity due to double bounce and direct return from vertical tree trunks and convex edges. In most cases, rough deposits produce an increase in intensity, while smooth deposits (e.g. from mudslides) exhibit specular reflection, and thus show decreased values. Landslides are less visible in cases with pre-event very rough ground, or mixed vegetation conditions. The conceptual model developed can aid interpretation of landslides in SAR imagery, and provide domain knowledge needed to train models for automatic landslide detection.

Keywords: change detection; time-series; landslide detection; land cover; Sentinel-1; backscatter; Google Earth Engine;

 doi:10.20944/preprints202302.0390.v1

1. Introduction

Landslides pose an increasing risk to the human population due to urban expansion into unstable areas, and an increasing frequency of extreme precipitation events (Froude and Petley, 2018; Gariano and Guzzetti, 2016; Hanssen-Bauer et al., 2009). Landslides frequently occur in conjunction with other types of natural hazards including earthquakes, floods, volcanic eruptions and tsunamis, particularly in areas with high hydrological or seismic risk (Casagli et al., 2017). Consequences may include loss of life, damages to infrastructure and property, blocked transport routes and dammed rivers which create further risk of flash flooding to downstream areas (Kjekstad and Highland, 2009).

Satellite-based emergency mapping can provide highly beneficial information to the humanitarian response community on the location, size and density of landslides. If performed within hours to days after an event, this information can improve situational awareness for responders, particularly if conducted as part of a coordinated mapping effort (Kedia et al., 2022; Williams et al., 2018). The increasing availability of medium to high resolution satellite images, combined with cloud-based high performance computing capabilities and automatic image detection methods have facilitated recent development of automated landslide detection models (Ghorbanzadeh et al., 2019; Prakash et al., 2021). Preliminary studies have yielded promising results at a local scale particularly with deep-learning methods. However, further development is needed to achieve automatic landslide detection models that perform well in diverse environments (Ganerød et al., 2023). Eventually, operational real-time monitoring and alert systems, such as presently exist for detection of illegal deforestation (Reiche et al., 2021), could be developed for landslides.

The majority of the existing landslide detection models rely on optical images and vegetation indices (Guzzetti et al., 2012). However, such analyses require cloud-free images and sufficient light conditions. In tropical and high latitude regions of the earth, persistent cloud cover, or seasonal darkness, can lead to delays of months before changes to the ground surface are observable in optical satellite images (Lacroix et al., 2018; Sudmanns et al., 2020). This is especially problematic for rapid detection of rainfall-triggered landslides, which typically occur under cloudy conditions (Williams et al., 2018).

Synthetic Aperture Radar (SAR) is cloud penetrating, therefore ground surface reflectance properties can be measured irrespective of cloud cover or illumination from the sun (ASF, 2022). However, compared to optical imagery, SAR data are more difficult to process and interpretation is less intuitive. This is due to a complex backscatter signal, speckle noise, phase wrapping and geometric distortions (Meyer, 2019). This presents an obstacle for geoscientists and other operators in using SAR backscatter images for rapid landslide detection (Handwerger et al., 2022; Mondini et al., 2019). Although there is a well-established community using In-SAR for monitoring slow-moving deep-seated landslides (Cigna et al., 2014; Mondini et al., 2021; van Natijne et al., 2022), the same methods are not frequently applied for detecting rapid landslides due to a lack of coherence in the phase component of the returning radar signal in vegetated areas (Mondini et al., 2019).

(Guzzetti et al., 2012) asserted that the real part (amplitude, or backscatter intensity) of the SAR signal should be exploited in order to detect ground changes caused by landslides. A review of 54 journal articles about landslide failure detection using SAR imagery, published between 1995 and 2020 (Mondini et al., 2021), found that literature on the exploitation of SAR for landslide event detection remains limited. They conclude that in principle, the available SAR amplitude images are well suited

 doi:10.20944/preprints202302.0390.v1

for landslide detection and mapping as the wavelength of the microwave SAR sensors is comparable to the length scales of morphometric elements typical of landslides. However, there remains a lack of understanding of the physical basis of backscatter response.

Recently, an increasing number of studies have begun to investigate the potential for using SAR-backscatter intensity change images for landslide detection and mapping using Sentinel-1 C-band SAR backscatter images. (Mondini et al., 2019) investigated the potential for detecting landslides in Sentinel-1 backscatter change images for 32 case studies. (Santangelo et al., 2022) explored how accurately two large single landslide events could be mapped using such images. Others, have used multi-temporal composites to improve landslide visibility in change images (Lindsay et al., 2022) and create heat maps of landslide density (Handwerger et al., 2022). (Burrows et al., 2022) used Sentinel-1 time-series to backdate monsoon-triggered landslides and explored the performance of different bands. There have also been a few attempts to automate this process using locally-trained deep-learning models (Ganerød et al., 2023; Nava et al., 2022).

While most of these studies test multiple band combinations (VV and VH) and orbit geometries (ascending or descending), interpretation of the spatial and temporal expression of landslides is still somewhat limited in detail. The majority of these studies focus on whether it is possible to detect, map and back-date landslides using SAR imagery. They do not systematically quantify the change in backscatter intensity, or relate it to the landslide type, morphometric elements, or environmental conditions. Most investigate landslides in densely forested areas, while areas with herbaceous or little to no vegetation, especially polar regions, are poorly represented (Mondini et al., 2021). Landslides are observed to produce both increases and decreases in backscatter intensity; however, a physically based explanation for these observations in relation to the ground properties is lacking.

In this study, we investigate the spatial and temporal signatures of different types of rapid landslides in diverse physiographical environments in 30 locations, using C-band SAR backscatter change images and time-series data. In doing so, we aim to improve understanding of how the physical changes to the ground surface relate to the change in backscatter intensity and scattering mechanisms, that determine the expression (pattern of increase or decrease) of landslides in SAR imagery. We consider the reflective properties of the pre-event ground surface, and the post-event landslide surface. In addition to identifying individual landslides, in some cases we are also able to distinguish separate morphometric features of landslides (i.e. scarps, sliding surfaces, deposits, and ponds) based on their specific expressions in the SAR change images. Based on these trends and new empirical data, we present a conceptual model that can be used to aid interpretation. The findings contribute towards developing standards for interpreting landslides in SAR backscatter change images. In addition, a diverse global dataset that can be used for training automatic landslide detection models was created.

The **research questions** are as follows:

1. What patterns and trends in the spatial and temporal expression of landslides in SAR backscatter intensity data can be identified from the 30 case studies?
2. Which factors control the visibility and expression of landslides in SAR data?

To answer these questions, we first consider how SAR theory can be related to landslide detection to identify the possible controlling factors. Then we examine the spatial and temporal signatures of

Preprints (www.preprints.org) | NOT PEER-REVIEWED | Posted: 22 February 2023 doi:10.20944/preprints202302.0390.v1

landslides, from 30 case studies with diverse landslide types and environmental conditions, and perform statistical analyses of the controlling factors. Based on the identified trends, and results from the statistical analyses, a physically-based conceptual model is presented to aid interpretation of landslides in SAR change images.

2. SAR backscatter theory applied to landslides

Changes to the ground surface caused by landslide erosion and deposition may change the surface roughness and dielectric properties of the ground surface and thus the intensity of backscatter. This information can be used to detect and map landslides. Several factors that can affect the visibility and expression of landslides in SAR backscatter intensity data are illustrated and described in this section. These include radar properties (wavelength (**λ**), polarisation and incidence angle), and surface properties (terrain elevation and geometric distortions, local incidence angle (LIA), roughness (relative to **λ**), and land cover type,) (Fung et al., 1992). Seasonal variations in vegetation or snow cover, and changes in moisture content, can also affect the backscatter intensity.

In Figure 1 (A), it is shown how the position of a landslide in the terrain relative to the sensor, determines whether the landslide signal will be affected by geometric distortions (including layover, shadow and foreshortening). It is seen that Landslide-I would be visible to the sensor, however distorted due to layover. While Landslide-II, would not be visible to the sensor as it is in the shadow zone. The distortion of Landslide-I can be corrected with a terrain correction, while the Landslide-II can be detected if images from both ascending and descending orbits are available.

In Figure 1 (B) the effect of the orientation of the landslide surface, relative to the sensor line of sight (LOS) is considered. Here, it is shown that the local incidence angle (LIA) affects the strength of the received backscatter signal, with surfaces with lower LIA generally returning stronger intensity signals than those with high LIA. The strength of the returned signal also depends on the ground surface properties, as will be shown in Figure 2, with surface scatters being more sensitive to the LIA than volumetric scatters. Figure 1 (C) illustrates how the wavelength of the sensor determines the height of irregularities (h [cm]) that the signal will be sensitive to, as well as the degree of penetration of vegetation and the elements of vegetation that the signal will interact with. Shorter wavelength signals (i.e. X- and C-band) are more sensitive to smaller changes in surface roughness (< 5cm), and are mainly reflected from the canopy. Longer wavelengths (i.e. L-band) are sensitive to larger scale changes in roughness (>10 cm), and penetrate leaves, thus are reflected from woody structures and the ground.

Preprints (www.preprints.org) | NOT PEER-REVIEWED | Posted: 22 February 2023 doi:10.20944/preprints202302.0390.v1

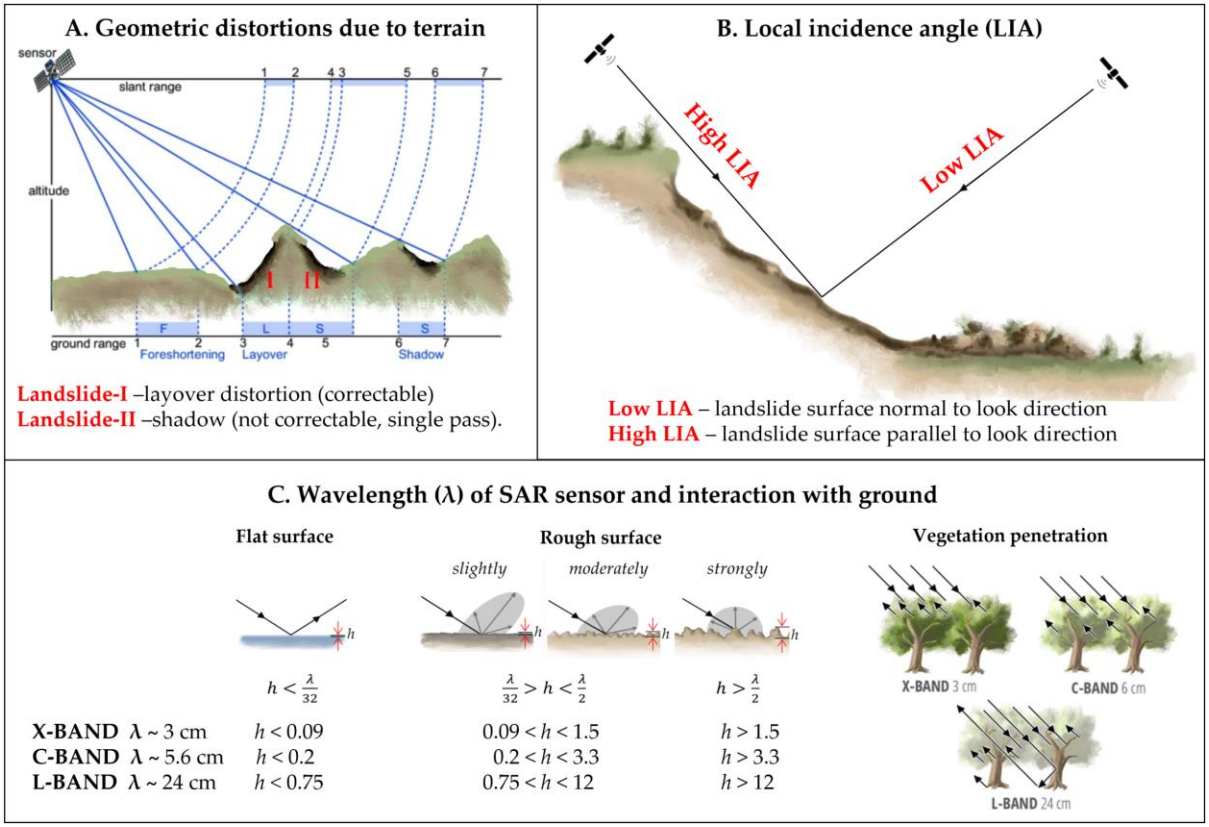

Figure 1 Factors affecting the expression of landslides in SAR data that remain static over time. These include the position of the landslide within the terrain relative to **(A)** terrain features, and **(B)** the sensor line of sight (LOS), and **(C)** the wavelength of the SAR signal (λ). Modified from (A) (Tempfli et al., 2009), (B) (Lindsay et al., 2022), (C) (Kellndorfer et al., 2019). The roughness is relative to the wavelength, h is the height of surface irregularities.

In Figure 2 (D), different ground-cover types and their associated scattering mechanisms are shown. Here we see that the intensity of the received backscatter increases with increasing surface roughness, with flat surfaces (e.g. still water, or snow) with oblique LIAs, reflecting the signal specularly in accordance with Snell's law (Ulaby et al., 2019). As surface roughness increases, diffusivity increases and more of the signal is reflected in all directions, including back towards the sensor. Co-polarised bands (e.g. VV) are more sensitive to variation in surface roughness. For volumetric scattering as occurs in vegetation, in C-band, the canopy provides a strongly reflective surface, with most of the energy received reflected volumetrically within the upper few cm of the canopy. Cross-polarised bands (e.g. VH) are more sensitive to variation in vegetation (volume scattering). For areas with mixed types of scatters, i.e. herbaceous vegetation, agriculture, or areas with both herbaceous and woody vegetation, the strength of the received signal depends on (i) the degree to which the signal penetrates the vegetation, and (ii) the roughness of the underlying soil surface. For thin herbaceous vegetation (e.g. grass, peat, or low bio-mass crops) the underlying surface roughness determines the intensity of the backscatter received, while for ground with predominantly volumetric scatters (e.g. dense leafy crops, small bushes) the biomass of the vegetation will have a stronger effect on the intensity. Finally, double bounce scatterers (near-vertically inclined surfaces, e.g. cliffs, or exposed tree trunks) produce the highest received backscatter intensity, and as surfaces, these features are most strongly observed in co-polarised bands.

Preprints (www.preprints.org) | NOT PEER-REVIEWED | Posted: 22 February 2023 doi:10.20944/preprints202302.0390.v1

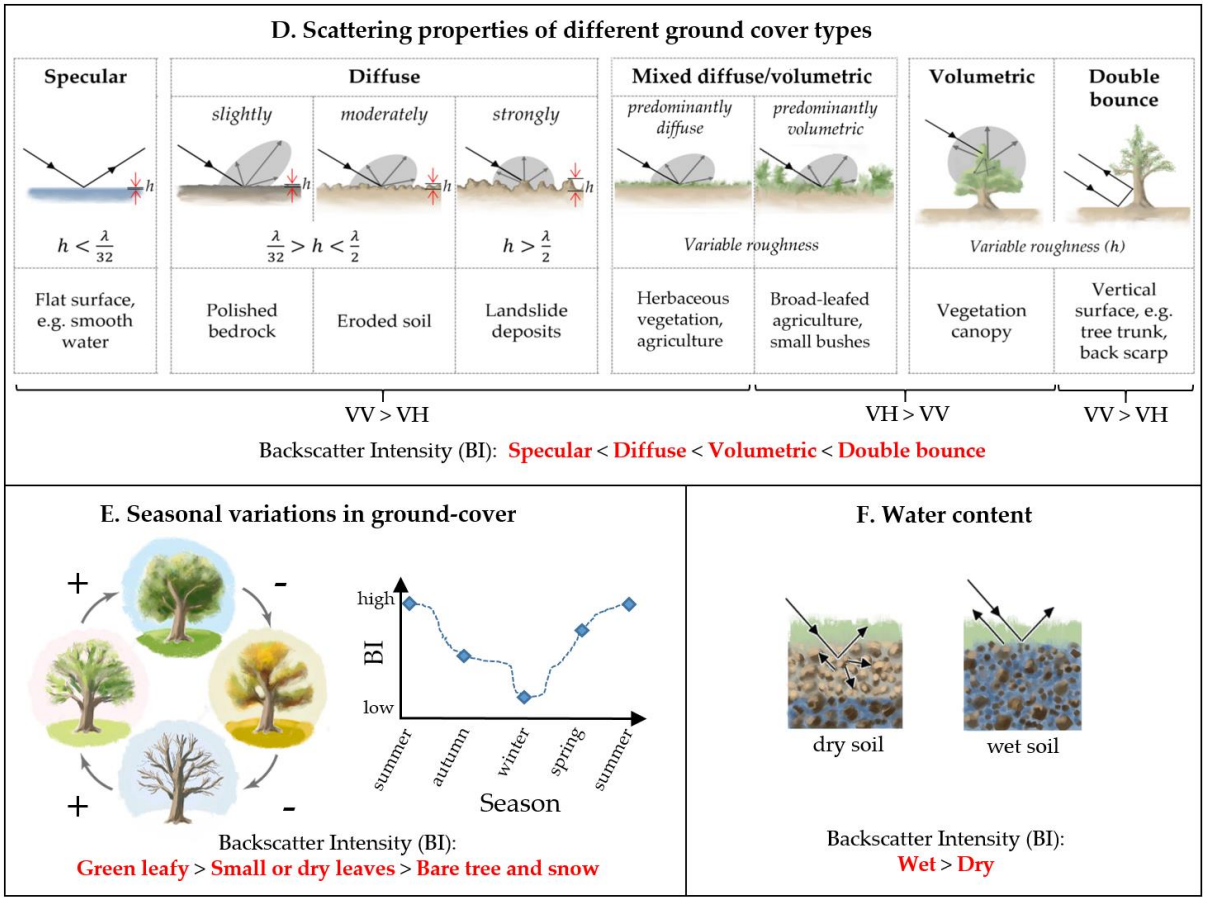

Figure 2 Factors affecting the expression of landslides in SAR data that may vary over time. These include **(D)** the type of ground cover and associated scattering mechanisms, **(E)** seasonal variations in ground cover, including vegetation changes and snow cover, and **(F)** water content

It is the change between the different types of ground cover types that determines the change in the observed intensity. For instance a change from a volumetric scatter (e.g. forest canopy) to a surface scatterer (e.g. soil surface) will result in a decrease in intensity and the edges of the remaining forest may also produce radar shadow (Bouvet et al., 2018). While for surfaces, an increase in roughness caused by deposition or erosion of the weathered soil surface, will produce an increase in intensity.

In Figure 2 (E) we see for a given ground cover type, the intensity can vary significantly if there are strong seasonal variations. For instance, intensity is highest when the leafy canopy reflects the SAR signal volumetrically, and is lower in autumn and spring when leaves are small or dry. Smooth snow reflects the signal away specularly, resulting in lower intensity. Finally in Figure 2 (F), we see that increased water content (of soil, snow, or vegetation) produces higher intensity than dry ground covers, due to increased conductivity, decreased penetration of the wave into the ground surface, and thereby increased reflectivity. The magnitude of intensity change that a landslide produces, will increase or decrease depending on seasonal variations of the preexisting ground cover.

By understanding how terrain, ground-cover, wavelength and polarisation produce backscatter signals of varying intensities, we can apply these ideas to predict how landslides may be expressed in change images and time-series data. Here we assume that landslides produce a change in ground surface cover, across an area of a size that is detectable within the resolution of the sensor. The types of ground-cover

 doi:10.20944/preprints202302.0390.v1

observed within a landslide area can be related to the morphometric features of landslides, landslide material, as well as failure mechanisms, and LIA.

As illustrated above, several factors can affect the expression of landslides in change images. The roughness of the landslide surface can vary depending on the type of material (soil or rock), soil particle coarseness (silt to gravel, and presence of rocks, boulders or other debris), and whether material was completely or partially eroded from the surface, and the deposition mechanism. The strength of the received backscatter for a smooth scarp or eroded surface (height of irregularities, $h < 0.2$ cm, for C-band) is strongly affected by the LIA. Scarps facing away from the LOS, that dip more steeply than the incidence angle, will be in a radar shadow zone and show very low intensity. The height of the scarp can be estimated based on the width of the shadow zone and the sensor incidence angle (Arnold et al., 2018). Smooth scarps with a high LIA (approximately parallel to LOS will either reflect the signal away from the sensor, resulting in a low intensity, while rough surfaces ($h > 3$ cm, for C-band) will scatter the signal diffusely and are less sensitive to the LIA. Scarps with a low LIA (approximately normal to LOS) will reflect more signal back towards the sensor. Landslide deposits are typically extremely rough surfaces consisting of transported material including rock and soil, water, and eroded vegetation. An exception are earth flows (mudflows), which consist of very fine particles and can form very smooth deposits. Where the topographic change is less significant, the specific change in surface properties will determine whether landslides are expressed by an increase or decrease in intensity. Landslides may dam rivers or streams, resulting in upstream swamps, ponds, or lakes. These areas will show strongly decreased intensity.

3 Case studies

A selection of 30 case studies from different locations, with varying terrain types, orientation and size, ground cover, climate zones, geological materials and failure mechanisms were systematically analysed in this study. The case studies were mostly identified from reports in 'The Landslide Blog' (https://blogs.agu.org/landslideblog/) (Dave Petley, 2022), or from news reports, or journal articles found by internet search. The location and dates of the investigated landslide events are shown in Figure 3, while the properties of the landslides and local environment are shown in Table 1.

The data used to describe the landslide properties was retrieved from the following sources:

- **Location and date:** literature (various sources, see appendix 1)
- **Landslide type and trigger:** from the reports describing the article, or classified from the descriptions and images according to (Hungr et al., 2014).
- **Landslide size and aspect:** the outline of the largest landslide in the study area was measured.

Preprints (www.preprints.org) | NOT PEER-REVIEWED | Posted: 22 February 2023 doi:10.20944/preprints202302.0390.v1

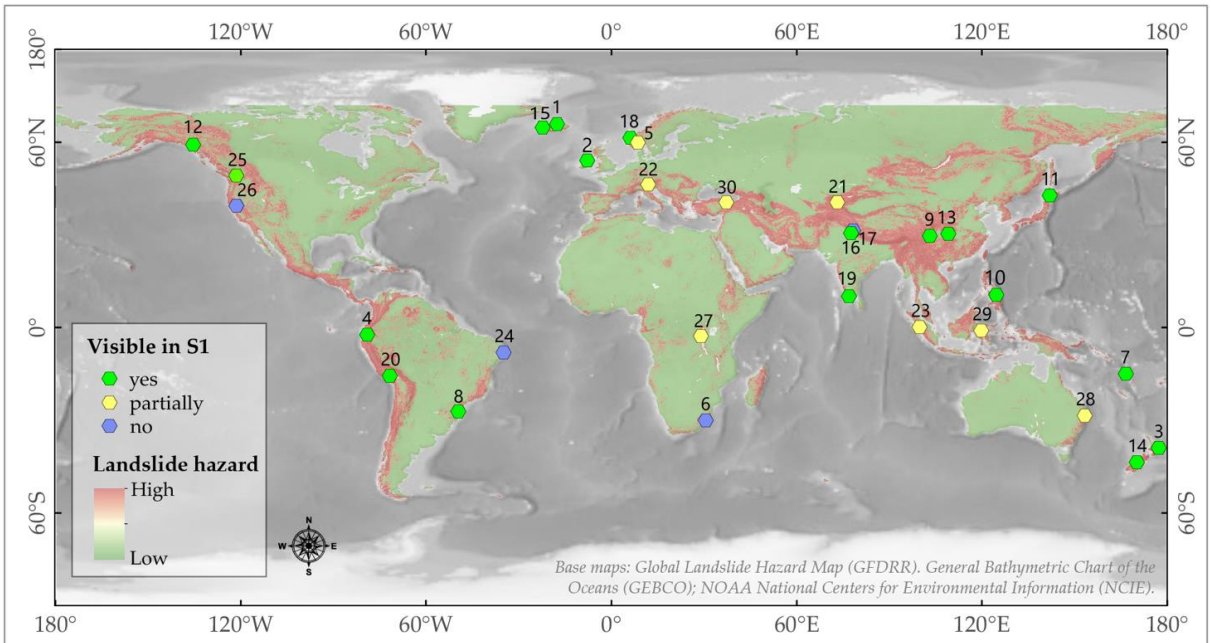

Investigated events (Location, event date, coordinates)

1. Iceland	2021-10-06	(-17.5558, 65.8674)	16. India	2021-07-25	(78.30762, 31.41447)
2. Ireland	2021-07-04	(-7.85187, 54.15745)	17. India	2021-07-30	(77.658109, 30.589764)
3. New Zealand	2022-03-27	(177.4694, -38.9681)	18. Norway	2019-04-28	(8.6385996, 59.84685)
4. Ecuador	2021-02-12	(-78.93655, -2.2895)	19. India	2020-08-06	(77.01188, 10.166)
5. Norway	2019-07-30	(6.11699, 61.51734)	20. Peru	2020-06-16	(-71.685998, -15.66025)
6. South Africa	2022-04-12	(30.69701, -29.89816)	21. Kyrgzstan	2017-04-29	(73.290135, 40.587722)
7. Vanuatu	2020-04-06	(166.63854, -14.9281)	22. Italy	2019-11-23	(8.434000, 44.295000)
8. Brazil	2020-04-06	(-49.60777, -27.0774)	23. Indonesia	2022-02-25	(99.99442, 0.11412)
9. China	2021-04-05	(103.15055, 29.66474)	24. Brazil	2022-05-26	(-34.958299, -8.120723)
10. Phillipines	2022-04-10	(124.85286, 10.67658)	25. Canada	2021-11-14	(-121.67202, 49.31537)
11. Japan	2018-09-06	(141.966, 42.7876)	26. USA	2021-11-24	(-121.38802, 39.86029)
12. USA	2019-12-02	(-135.41194, 59.22035)	27. Burundi	2019-12-05	(29.080122, -2.619565)
13. China	2020-07-21	(109.29972, 30.36592)	28. Australia	2022-02-28	(153.39578, -28.51734)
14. New Zealand	2022-02-03	(170.17485, -43.57436)	29. Indonesia	2018-09-28	(119.91418, -0.93951)
15. Iceland	2022-02-02	(-22.109811, 64.78794)	30. Turkey	2019-05-16	(37.378026, 40.670806)

Figure 3 Map of case study locations and event dates. Base map: Landslide Hazard Map (GFDRR, 2023)

For each set of coordinates in Figure 3, values from the following maps were extracted using Google Earth Engine or ArcMap:

- **Geology:** Generalised Geology of the World, WMS V 1.3.0 (Chorlton, 2007),
- **Climate zone:** World Map of the Köppen-Geiger climate classification (Kottek et al., 2006)
- **Mean annual rainfall:** WorldClim BIO Variables V1 (Hijmans et al., 2005)
- **Land cover classification:** CORINE (EEA/Copernicus, 2012) and Copernicus Global Land Cover (Copernicus, 2019)

Preprints (www.preprints.org) | NOT PEER-REVIEWED | Posted: 22 February 2023 doi:10.20944/preprints202302.0390.v1

Table 1: Properties of the investigated landslides and their local environment. The visibility of the landslides are also presented according to their assigned set. Set 1: not visible, set 2: partially visibly, recognisable only knowing a priori the location, and set 3: clearly visible.

	Landslide				Environment				Set
Location	**Type**	**T**	**Size L x W [km]**	**Aspect**	**Geology**	**K.G. Climate**	**Rainfall [mm/yr]**	**Land cover Gl / EU**	**1 No 2 Part. 3 Yes**
1. Iceland	DS	R	0.8 x 0.1	E	V	Cfc	672	Herb./ Moor	3
2. Ireland	PF	R	0.58 x 0.7	NW	S	Cfb	1358	Herb. / Peat	3
3. N. Zealand	DS	R	0.13 x 0.05	W	S	Cfb	1508	Herbaceous	2
4. Ecuador	EF	R	1.5 x 1.5	W-NW	S-V	Cfb	918	F|Unknown	3
5. Norway	DF, DA	R	0.11 x 0.03	mixed	M	Dfc	2285	Herbaceous	3
6. Sth. Africa	DF	R	0.5 x 0.2	W	M	Cfa	940	Herbaceous	1
7. Vanuatu	DS-DF	R	0.8 x 0.2	S	V	Af	3440	F|Broadleaf	2
8. Brazil	DF	R	1.6 x 0.02	NE	S	Cfa	1547	F|Broadleaf	2
9. China	DS-DF	R	1.34 x 0.92	S	S	Cwb	1297	F|Broadleaf	3
10. Philippines	MS	R	2.1 x 0.7	SW	S	Af	2915	F|Broadleaf	3
11. Japan	DS, DF	ER	0.22 x 0.13	mixed	S-V	Dfb	1131	F|Broad. dec.	3
12. USA	DA	R	1.7 x 0.18	N	P	Dsb	1282	F|Needle	3
13. China	DS	R	1.2 x 0.3	S	S	Cfa	1409	F|Unknown	3
14. N. Zealand	RA	R	1.8 x 0.28	SE	S	ET	4222	Snow	3
15. Iceland	RA	R	2.4 x 1.7	SE	V	Cfc	829	Herb. / Grass	3
16. India	RF	R	0.68 x 0.15	SW	M	Cwb	824	Herbaceous	1
17. India	DS	R	0.34 x 0.2	SE	S	Cwa	2183	F|Unknown	2
18. Norway	SF	S	1.35 x 0.95	E	V	Dfc	974	Herb. / Rock	1
19. India	DF	R	1.2 x 0.12	S	P	Am	2848	F|Needle	3
20. Peru	EF	U	0.6 x 1	NE	S-V	Dsb	506	Herbaceous	3
21. Kygysztan	CCS-EF	RS	5 x 0.6	NE	S	ET	394	Herbaceous	2
22. Italy	DF	R	0.35 x 0.07	SE	S	Dfc	886	Agriculture.	2
23. Indonesia	DF	E	6 x 0.3	NE	V	Af	2775	F|Broadleaf	2
24. Brazil	DS	R	0.06 x 0.03	SE	S	Am	1678	Urban	1
25. Canada	DF	R	0.85 x 0.32	SE	S-V	Cfb	1712	F|Needle	3
26. USA	RF	U	0.09 x 0.06	W	P	Csb	1560	Shrub	1
27. Burundi	DS, DF	R	0.4 xx 0.3	mixed	M	Aw	1519	F|Unknown	2
28. Australia	DS, DF	R	0.8 x 0.04	S	S	Cfa	2031	Agriculture	2-3
29. Indonesia	SLS	E	2.1 x 1.1	W	P	Af	1534	Urban	2
30. Turkey	RS	U	0.5 x 0.3	SE	S-V	Cfb	626	Agriculture	3

Acronyms: Type (according to Hungr et al., 2014): RF. Rock fall, RS. Rock rotational slide, DS. Gravel/sand/debris slide, CCS. Clay/silt compound slide, SLS. Sand/silt liquefaction spread, RA. Rock avalanche, DF. Debris flow, MF. Mud flow, DA. Debris avalanche, EF. Earthflow, PF. Peat flow, SF. Slush flow. **Trigger (T)**: R – rainfall, E-earthquake, S – snowmelt, U - unknown. **Geology:** S - mainly sedimentary terrane, P - plutonic terrane, M – metamorphic, S-V - mixed sedimentary-volcanic terrane, V - mainly volcanic terrane. **K.G. Climate zone:** A (Tropical) + f (Rainforest), m (Monsoon) w (Savanna, Dry winter) s (Savanna, Dry summer); C (Temperate) + w (Dry winter), f (No dry season), s (Dry summer) ||a (Hot summer), b (Warm summer), c (Cold summer); D (Continental) + w (Dry winter), f (No dry season) s (Dry summer) ||a (Hot summer) b (Warm summer) c (Cold summer) d (Very cold winter); E (Polar) + T (Tundra), F (Eternal frost (ice cap)). **Land Cover: Gl (Copernicus Global Land Cover):** F - Forest | dec. – deciduous, broadleaf. **Land cover: EU (CORINE Land Cover):** Grass - Natural grassland, Moor - Moors and heathland, Rock - Bare rocks, Peat - Peat bogs.

As shown in Table 1, of the 30 events included in this report, the most common types were debris slides and debris flows, with eight in each category. Half of the events had rapid flow type failure mechanisms. The next most frequent failure mechanism was sliding, including 10 events. Nearly all the landslides were rainfall triggered (25/30), with the remaining being earthquake triggered or unknown.

Preprints (www.preprints.org) | NOT PEER-REVIEWED | Posted: 22 February 2023 doi:10.20944/preprints202302.0390.v1

In terms of size, 10 were less than 0.1 km^3, and 12 were between 0.1 and 1 km^3. The remaining eight events were between 1-5 km^3. 12 different climate classes were included, with seven case studies in tropical climates (A), 15 in temperate climates (C), six in continental climates, and two in polar climates (E). For geology, 13 cases were located in sedimentary bedrock, five in volcanic, and four cases each had metamorphic, plutonic or mixed sedimentary-volcanic terrane bedrock. The mean annual rainfalls varied from 394 mm/yr in Kyrgyzstan (#21), to 4222 mm/yr in New Zealand (#14). The land cover types using the Copernicus Global Land Cover map included 15 cases in forest, 12 in herbaceous, cropland or shrubs, two in urban areas, and one in snow/ice.

4 Methods

The input data, pre-processing, visualisation and interpretation methods are described in the following section. The Sentinel-1 SAR change images and time-series were made for each case study using Google Earth Engine, (GEE), (Gorelick et al., 2017). Date ranges for the pre- and post-event image collections, and coordinates of the approximate event location were used as filter conditions, to produce pre- and post-event image stacks of both Sentinel-1 GRD product (Ground Range Detected) and Sentinel-2 (Level 2A) images. Time-periods of one, two, or 12 months either side of the event date were used, depending on the local image acquisition frequency, and seasonality. The date ranges and coordinate locations used for each case study (along with the change images produced) are provided in the electronic supplement. Pre- and post-event image composites were produced from the image stacks, for a 4 km^2 area about the defined point.

The Sentinel-1 images, available on GEE are available pre-processed (calibrated and ortho-corrected) in 10 m resolution. Image stacks were produced by filtering for ascending or descending obit pass, VV or VH receiver polarisation, and Interferometric Wide (IW) instrument swath mode. A terrain correction (Vollrath et al., 2020) was applied to each image in the stack using either a volumetric or a surface model, depending on the land cover type. For most cases, the 30 m resolution Shuttle Radar Topography Mission (SRTM) digital elevation model (DEM) available within GEE was used. However, local DEMs were needed for the Icelandic case (link: https://gee-community-catalog.org/projects/iceland_dem/, accessed: 11 December 2022) and Norwegian cases (https://hoydedata.no/LaserInnsyn2/, accessed: 11 December 2022). The Sentinel-1 composites were created by taking the median of the terrain-corrected image collections, and change images (post-minus pre-event image composite) produced from these.

For Sentinel-2, a Normalised Difference Vegetation Index (NDVI) band was added to each image in the pre- and post-event stacks, then a greenest-pixel composite was created (maximum NDVI), using the quality-mosaic tool. An NDVI change image (dNDVI) was then produced by subtracting the pre- from the post-event composite. These are shown in Figure 4. The dNDVI images were used for verification purposes and digitising outlines of the landslides.

Preprints (www.preprints.org) | NOT PEER-REVIEWED | Posted: 22 February 2023 doi:10.20944/preprints202302.0390.v1

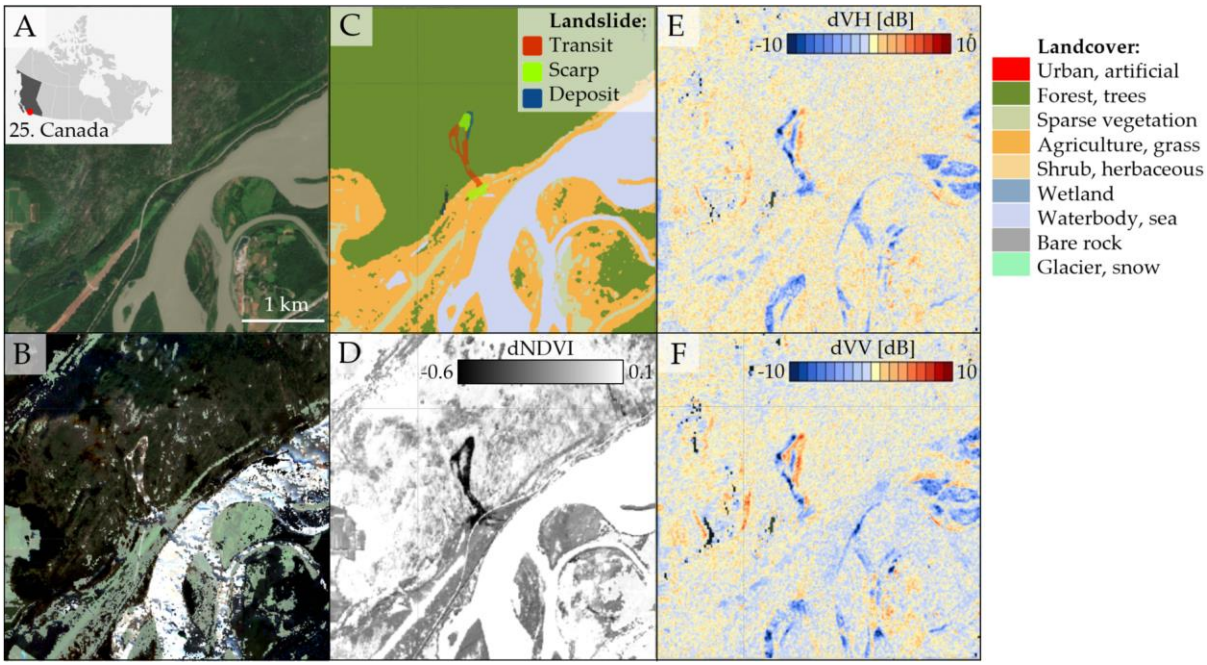

Figure 4 Data preparation for statistical analyses, showing case study 25. Ruby Creek landslide, British Columbia, Canada (14 November 2021). Input images including: A) Sentinel-2 Pre-event least cloudy image. B) Sentinel-2 Post-event greenest-pixel composite. C) Pre-event land cover produced using machine learning classifier, with pre-event Sentinel-1, -2 and DEM as input. D) Change in Normalised Difference Vegetation Index (dNDVI). E) Sentinel-1 Change in backscatter intensity (ascending VH). F) Sentinel-1 Change in backscatter intensity (ascending VV).

From the Sentinel-1 change images, it was determined firstly, whether the investigated landslides were visible. The case studies were assigned a set-number, following the approach by (Mondini et al., 2019): Set 1: not visible, set 2: partially visibly, recognisable only knowing a priori the location, and set 3: clearly visible. If visible (set 2 or 3), time-series plots were produced. This involved selecting a point within the landslide, and point adjacent to the landslide with similar but undisturbed vegetation. From these points, 30 m^2 square polygons were generated, and five years of terrain corrected S1 time-series data, with median backscatter intensity [dB] for ascending-VV and –VH, and descending-VV and -VH, were exported.

Next, in order to investigate the factors that influence the expression of landslides in the change images, plots of LIA, land cover class and backscatter intensity values were made. This involved manually mapping the landslide polygons for each case study, exporting the Shapefiles along with Geotiff raster images for each case study, and finally extracting and plotting the pixel values from within the polygons. The LIA was already calculated as part of the terrain correction algorithm, so the original set of outputs (VV, VH and angle) was modified to also include the LIA. Where possible, landslides were mapped according to morphometric feature class (scarp, transit or deposit zone). Additional ground-based or drone images of the landslides (internet search, journal articles) showing the shape of the landslide were used to identify these separate features, although there remained uncertainty in the exact boundaries. If no additional information was available to identify the morphometric features, then the entire landslide body was mapped in the transit zone class as the default, as this includes both erosion and deposition.

For the land cover class, existing land cover maps (Copernicus Global Land Cover, CORINE, Dynamic World) were first examined. These were deemed to be not of high enough accuracy at the pixel level

Preprints (www.preprints.org) | NOT PEER-REVIEWED | Posted: 22 February 2023 doi:10.20944/preprints202302.0390.v1

for statistical analyses. Therefore, we produced our own locally-trained land cover maps. For each case study a machine-learning based land cover classification was performed using the ee.smile.CART algorithm (Classification and Regression Tree) in GEE (Breiman et al., 2017). These were trained using a Sentinel-2 image with minimal cloud cover from before the event, along with the DEM, and pre-event Sentinel-1 composite images (VV and VH polarisation). The classifier was trained by manually selecting points within the following classes; Urban, artificial; Forest, trees, Scrub, herbaceous; Pasture, grass; Sparsely vegetated; Water body, sea; Wetland; Bare rocks; and Glacier, snow. A minimum of 10 points were selected in each of the classes present. Then the images were sampled at the selected points, the classifier was trained. The classification was thereafter performed over the entire area of interest and results viewed. If the classification was not satisfactory (judged by visual comparison of the results with the higher resolution base satellite images) then additional training points were added, or input data modified. The process was repeated until a satisfactory land cover map was achieved.

Finally, for each case study the following data was exported: 1) landslide polygons, (2) geotiff raster images including the pre-processed Sentinel-1 bands from ascending and descending mode where available (preVV, postVV, dVV, preVH, postVH, dVH, LIA) along a band of the land cover class. The pixel values within each of the landslide polygons were extracted to produce a dataset consisting of approximately 300,000 pixels. Using Seaborne (version 0.12.2) violin plots and 2-dimensional histogram plots were produced to display the distribution of the data. The default settings were used, except for the histograms where the argument stat="percent" was used instead of "count" (Waksom, 2022a, 2022b).

5 Results:

Over 1000 landslides were digitized from the 30 case studies. During this process we identified predictable patterns in the expression of landslides in SAR backscatter change images related to the different morphometric features of the landslides (scarp, transit zone and deposit zone) and land cover type, and performed statistical analyses of the pixel values from the landslides. Here, we present an overview of the trends that were identified, and present evidence from individual cases and the statistical analyses that show how different factors, including land cover and landslide orientation relative to the sensor, control this expression.

5.1 Trends identified in the expression of landslides in SAR data

Some examples of the trends identified are shown with contextual photos in Figure 5, SAR difference images in Figure 6 with five-year time-series plots in Figure 7. These trends are summarised as follows:

(A) Scarp: The expression of scarps varied depending on the look direction, with scarps angled away from the sensor look direction producing an abrupt decrease in backscatter intensity in both dVV and dVH images, while scarps facing towards the sensor produced slightly to moderately increased backscatter intensity. The time-series plots in Figure 7 show that the decrease was most clear in VV polarised data, with a magnitude of 7 to 12 [dB]. In some cases (seen quite clearly in case 20 in Peru), an edge of increased back scatter intensity was also observed slightly behind the scarp on the far side of the landslide from the sensor. Rock fall scarps were not clearly distinguishable in the cases we examined.

(B) Transit zone in herbaceous vegetation: the most easily distinguishable landslides were those that occurred in herbaceous vegetation (e.g. tundra, peat, grass, cultivated land). These

 doi:10.20944/preprints202302.0390.v1

produced strong increases in backscatter intensity shown in time-series (Figure 7), most clearly seen in VV polarised data, in the order of 7 to 10 dB in the time-series data.

(C) Transit zone in forested area: a more complex, but quite distinct, pattern of backscatter intensity change was observed in most of the landslides that occurred in forested areas, seen most clearly in VH polarisation. As with the scarps, the pattern depends on the look direction of the sensor. For the cases shown in Figure 6 (including cases 5, 9, 10, 12, 23, and 25) it can be seen that moving away from the sensor - there is a sequence with first decreased backscatter intensity along the edge of the landslide closest to the sensor, and increased backscatter intensity on the far edge of the landslide. For wider landslides there may be a zone with moderately increased or decreased backscatter intensity in the centre of the transit zone. The decreases shown in the time-series plots are around 4 to 8 db.

(D) Deposits: in most of the cases we observed, deposits were observable by a moderately to strongly increased backscatter intensity (in VV polarisation) as seen in cases 2 and 14. Although in some specific cases the deposits were observable by areas of decreased backscatter intensity, as seen in cases 10 and 25. From the contextual photos in Figure 5, it appears that the deposits with decreased backscatter intensity relate to cases where fine sediments settled from still water caused by drainage blockage. Whereas, those showing increased backscatter intensity appear to relate to deposits consisting of coarser materials inferred to be deposited more rapidly from the turbulent landslide flow.

Preprints (www.preprints.org) | NOT PEER-REVIEWED | Posted: 22 February 2023 doi:10.20944/preprints202302.0390.v1

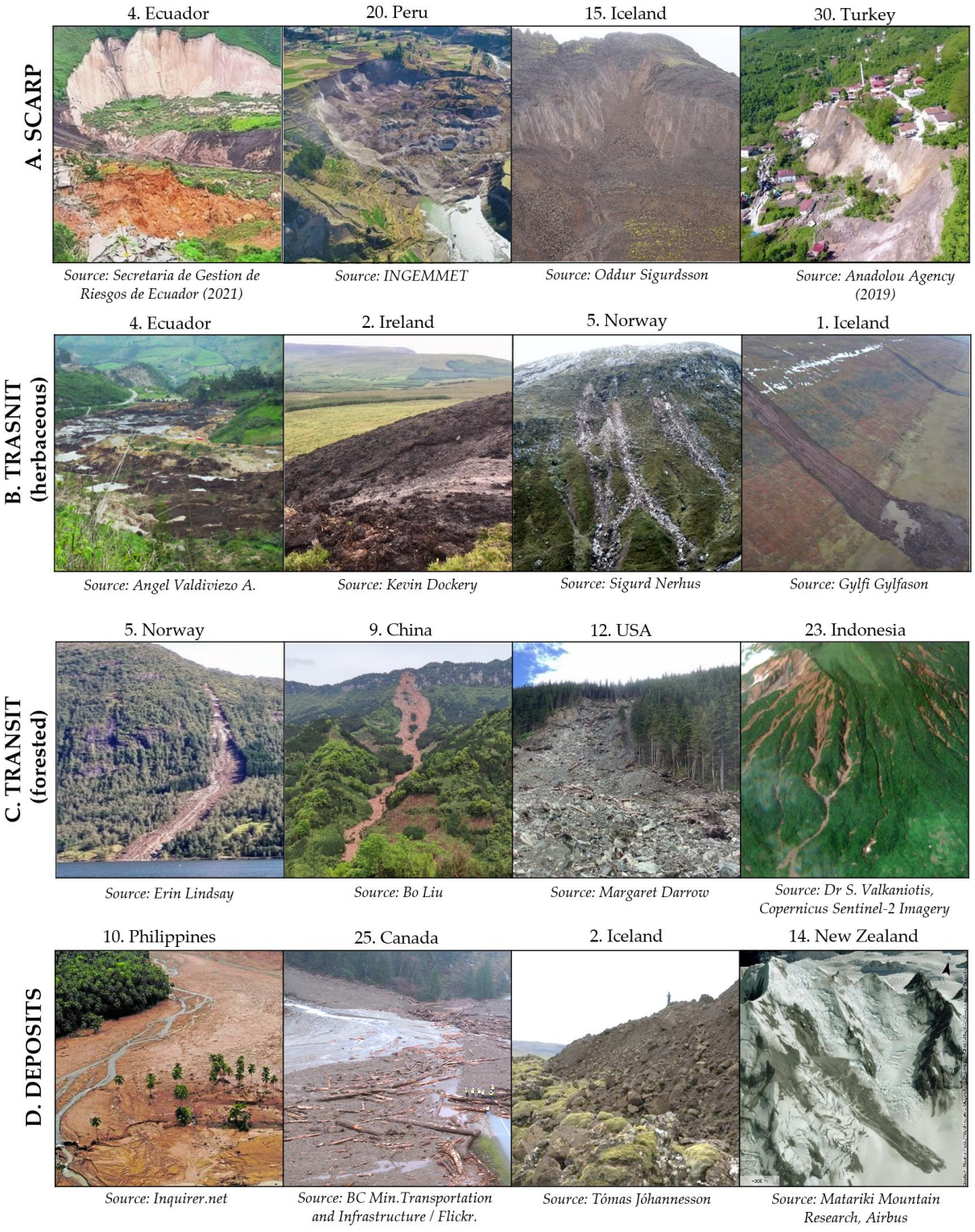

Figure 5 Context images corresponding to the landslides shown in Figure 7 and Figure 8, showing a variety of landslide types and environmental settings.

Preprints (www.preprints.org) | NOT PEER-REVIEWED | Posted: 22 February 2023 doi:10.20944/preprints202302.0390.v1

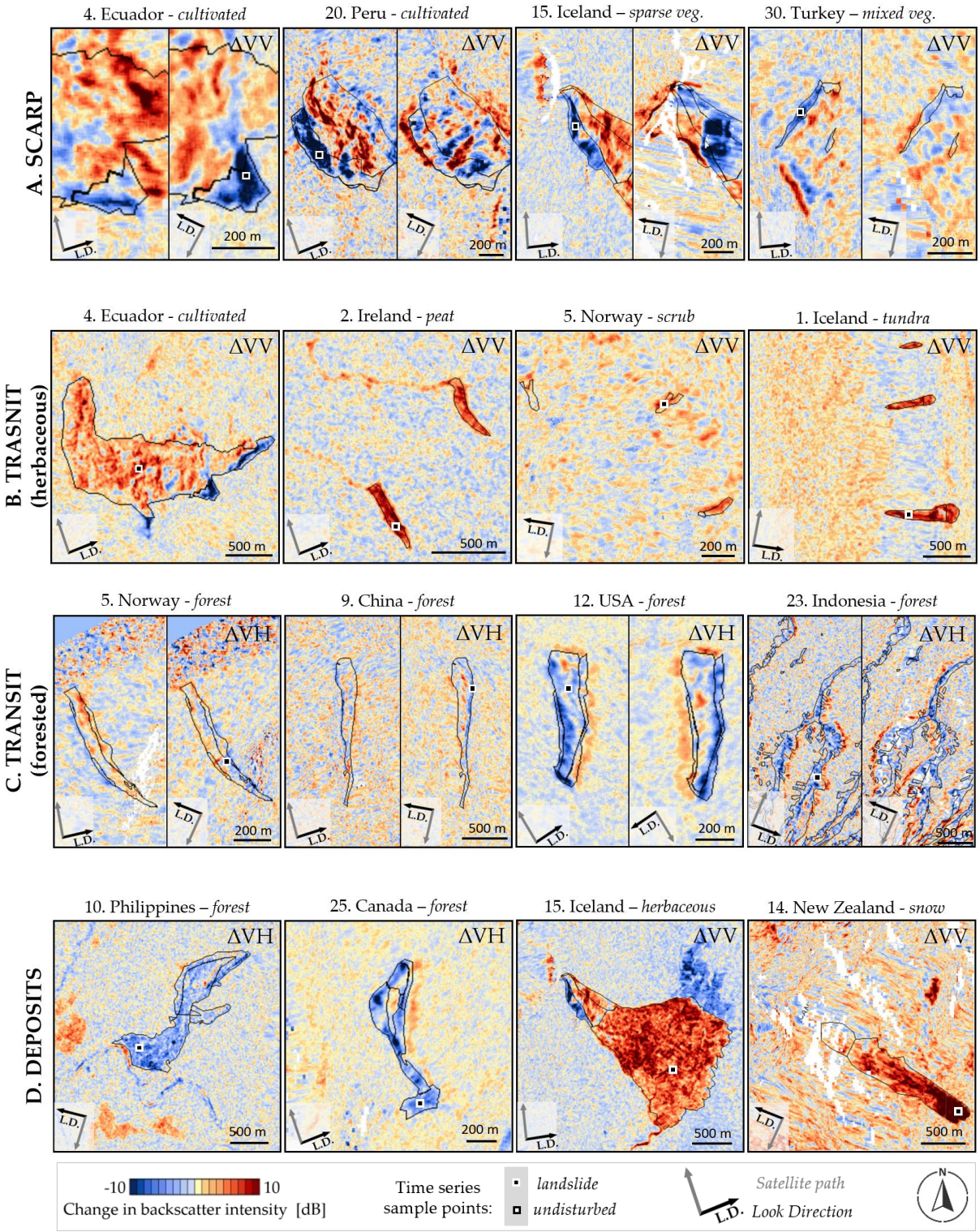

Figure 6 Collection of backscatter intensity change images showing a selection of landslides, demonstrating the trends identified during systematic mapping of landslides in all 30 case studies shown in Figure 3. The change images are produced from pre- and post-event median composite (from stacks consisting of 1 to 12 months of images, see appendix for details) of terrain-corrected Sentinel-1 SAR images. Center coordinates and dates of the landslides are provided in Figure 3.

Preprints (www.preprints.org) | NOT PEER-REVIEWED | Posted: 22 February 2023 doi:10.20944/preprints202302.0390.v1

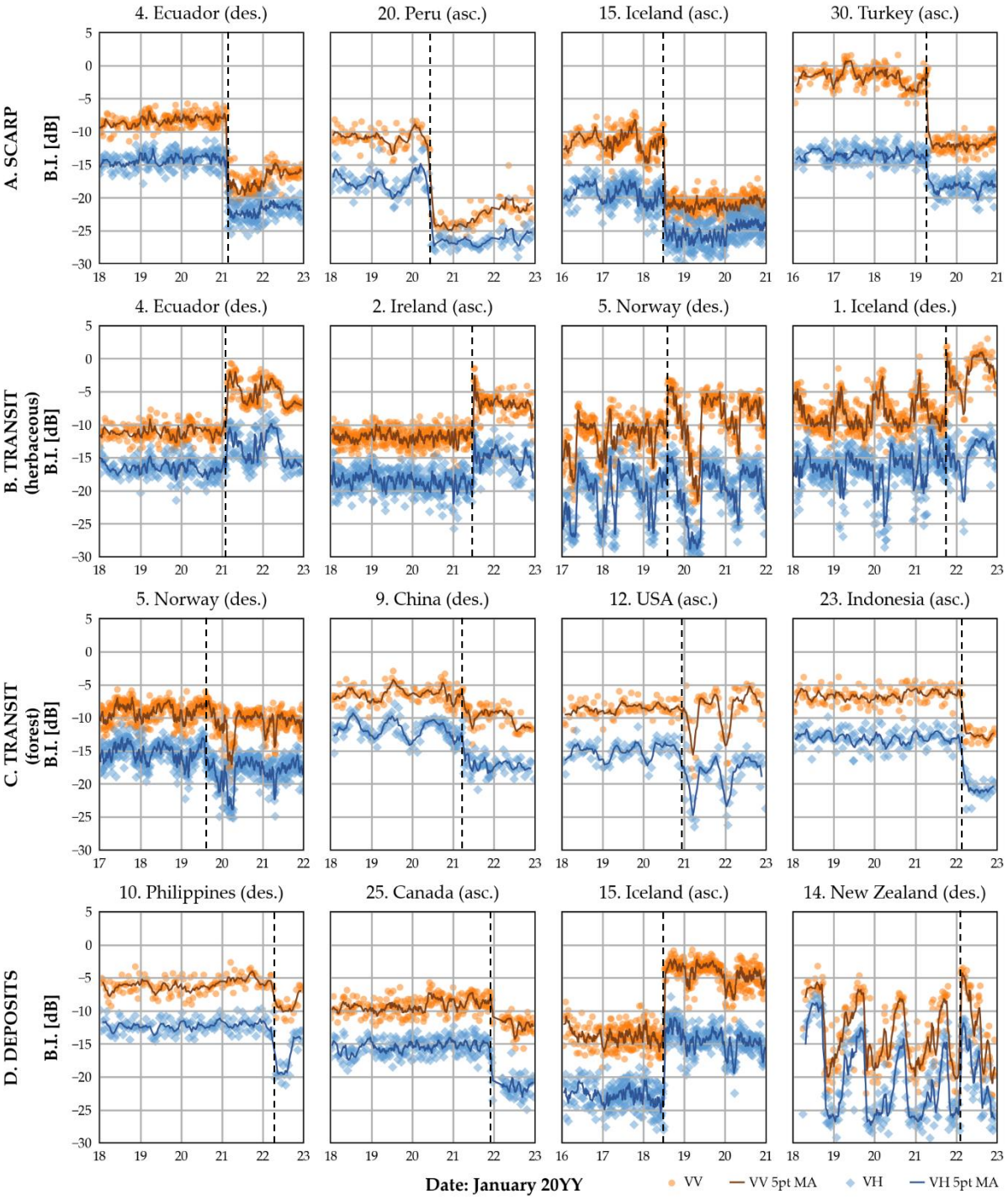

Figure 7 Five-year time-series plots of mean backscatter intensity (B.I.) in VV and VH polarisation, sampled from a 30 x 30 m patch within the landslide body. The location of the sample patches are shown in Figure 7. Landslides can be observed by an abrupt change in the seasonal cycle of backscatter intensity. The black dashed lines show when the landslide occurred. Event dates for each case are provided in Figure 3.

5.2 Factors controlling the expression of landslides in SAR data

The factors identified in the theory section as being relevant to the visibility and expression of landslides in SAR backscatter intensity change images included: terrain elevation and geometric distortions, local incidence angle (LIA), wavelength, land cover types, seasonal variations and water content. With the exception of wavelength, which was fixed in this study (C-band), the role of each of the factors is

Preprints (www.preprints.org) | NOT PEER-REVIEWED | Posted: 22 February 2023 doi:10.20944/preprints202302.0390.v1

considered based on the results of systematic mapping of the landslides along with pixel-based statistical analyses.

5.2.1 Large scale terrain features and geometric distortions

Geometric distortions were considered to have been a major limitation to landslide visibility in six of the cases (including 7. Vanuatu, 8. Brazil, 14. New Zealand, 26. USA, 27. Burundi, and 28. Australia). This was particularly problematic if only one orbit pass was available. In the Burundi case, although two orbit passes were available, a significant area was affected by foreshortening in both the ascending and descending images (see Figure 8), which appears as stretched pixels when corrected and distorts the landslide signatures significantly. This is problematic for areas with steep narrow valleys. Shadow zones were not as problematic as expected for large scale terrain features (e.g. the 4000 m high mountains in Case 14 from New Zealand, see Figure 7. Most of the shadow zones were related to the presence of medium scale topographic features, such as cliffs.

5.2.2 Local incidence angle

The local incidence angle can have a strong impact on the expression of landslides in SAR data, as illustrated in Figure 6. In particular, this is observed for landslides with significant scarps and those that occur in forested areas where the appearance of the landslide varies significantly depending on the sensor direction. Some of the landslides triggered by the earthquake in Hokkaido, Japan, shown in Figure 9, show how strongly the expression of landslides can vary depending on the orientation of the landslide surface.

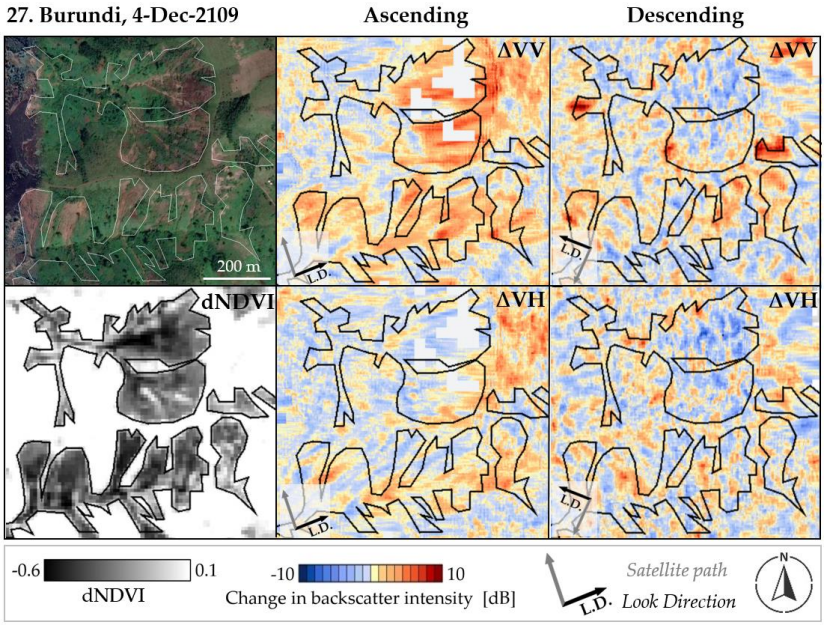

Figure 8 Landslide visibility was reduced in the Burundi case due to geometric distortions, as well as unfavorable mixed vegetation conditions. Black areas show shadow distortion, while the stretched pixels are presumably affected by foreshortening. Outlines were drawn based on the Sentinel-2 dNDVI image.

Preprints (www.preprints.org) | NOT PEER-REVIEWED | Posted: 22 February 2023 doi:10.20944/preprints202302.0390.v1

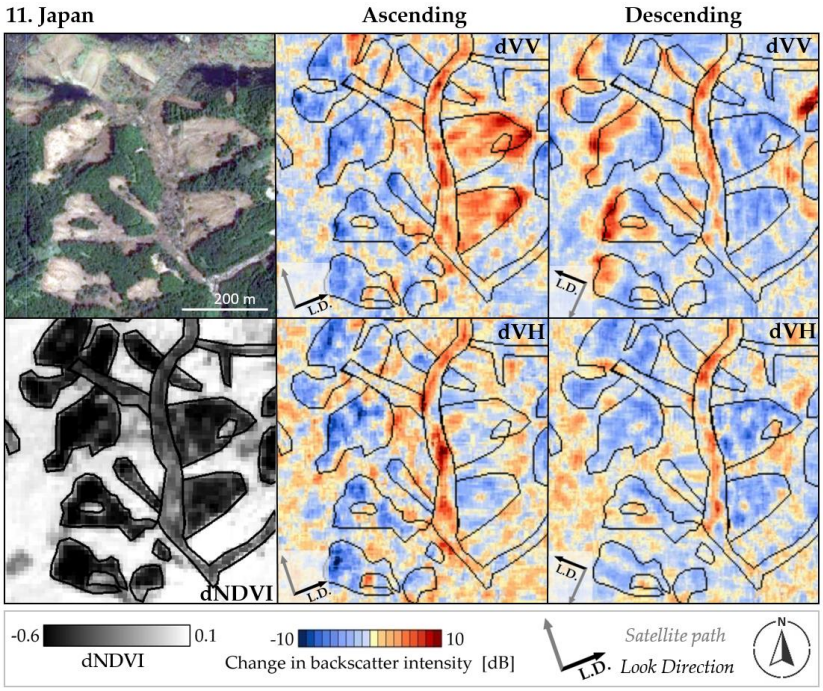

Figure 9 Landslides in forested area from Hokkaido, Japan (case 11) showing strong variation in expression in backscatter intensity change images depending on the orientation of the landslide surface. Outlines were drawn based on the Sentinel-2 dNDVI image.

The landslide scarps to the west of the central valley are mainly sloping down towards the east, in a similar direction to the look angle of the sensor on the ascending path (high LIA). In both the dVV and dVH ascending images, these western landslides show decreased backscatter intensity at the location of the back scarps. While the landslides to the east of the central valley facing approximately normal to the sensor (low LIA) show a strong increase in the dVV image at the location of the back scarp and a moderate increase in the mid slope. By contrast, in ascending dVH these eastern landslides show moderately decreased backscatter intensity in both the mid slope and towards the back scarps. A similar, but reversed pattern can be observed in the descending images. The local incidence angle appeared to be less relevant for landslides that occurred in herbaceous vegetation and for deposit zones. In Figure 9, the deposit zone in the centre of the valley shows an increase in all of the change images.

The 2D-histograms in Figure 10 show the spread of pixel values from within the mapped landslides depending on the LIA, and separated according to land cover type, landslide morphometric feature and polarisation. Although, there were relatively few data points in the scarp category, some strongly increased backscatter intensity values are observed at low LIA within forested examples, both for VV and VH polarisations. This fits with the observations from the Japanese case study shown in Figure 9. In the non-vegetated transit zone, and herbaceous deposits plots, there appears to be a weak trend of increasing dVV and dVH values with increasing LIA for the middle LIA values. However, there are a lack of points sampled at low and high LIAs in these categories. For the remaining plots there does not appear to be any clear relationships between the change in backscatter intensity values and the LIA.

5.2.3 Changes between ground cover types

The change in ground cover and associated scattering mechanisms depends both on the pre-event land cover, as well as the post-event texture of the ground produced by the landslide. From the 2D-

Preprints (www.preprints.org) | NOT PEER-REVIEWED | Posted: 22 February 2023 doi:10.20944/preprints202302.0390.v1

histograms in Figure 10, it can clearly be seen that deposits tend to produce increased back scatter intensity in all land cover classes, although the difference is greater in herbaceous and non-vegetated classes. While from the transit plots in forested areas, that landslides generally produce a decrease in backscatter intensity.

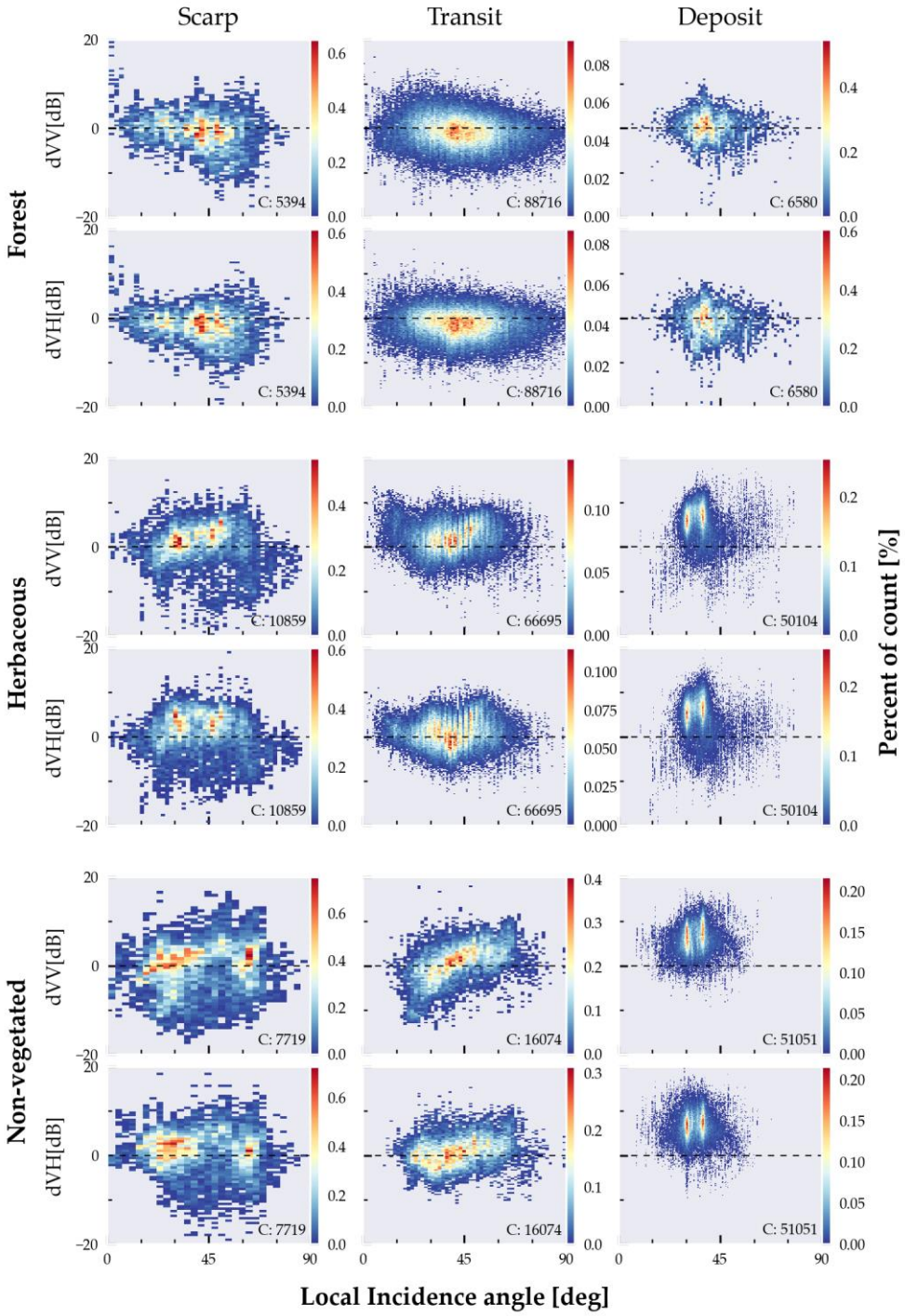

Figure 10 2D Histograms of data points sampled from within the landslides polygons (columns). Separated according to land cover class, and polarisation. Shows the distribution of the pixel values LIA vs change in backscatter intensity. In the herbaceous category, land cover classes including sparse vegetation, pasture, grass, wetland, scrub and herbaceous were combined. For non-vegetated urban, artificial water bodies, bare rocks, and

Preprints (www.preprints.org) | NOT PEER-REVIEWED | Posted: 22 February 2023 doi:10.20944/preprints202302.0390.v1

glacier and snow were combined. C: indicates the pixel count. Note that the LIA is calculated from the pre-event DEM.

Figure 11 shows increasing backscatter intensity of deposits from four cases. Post-event deposits show variation depending on the material, variation between the medians of 4 dB. The backscatter intensity increases with increasing material size (10. mainly fines, 5. mixed fine and coarse, 9. mixed with vegetation debris, to 11. rock and boulders). Note that the deposits in cases 5, 10, and 11, occurred on mainly flat or shallowly sloping areas, while those in 14 are from a slope with a lower incidence angle, therefore the values may be slightly higher due to this.

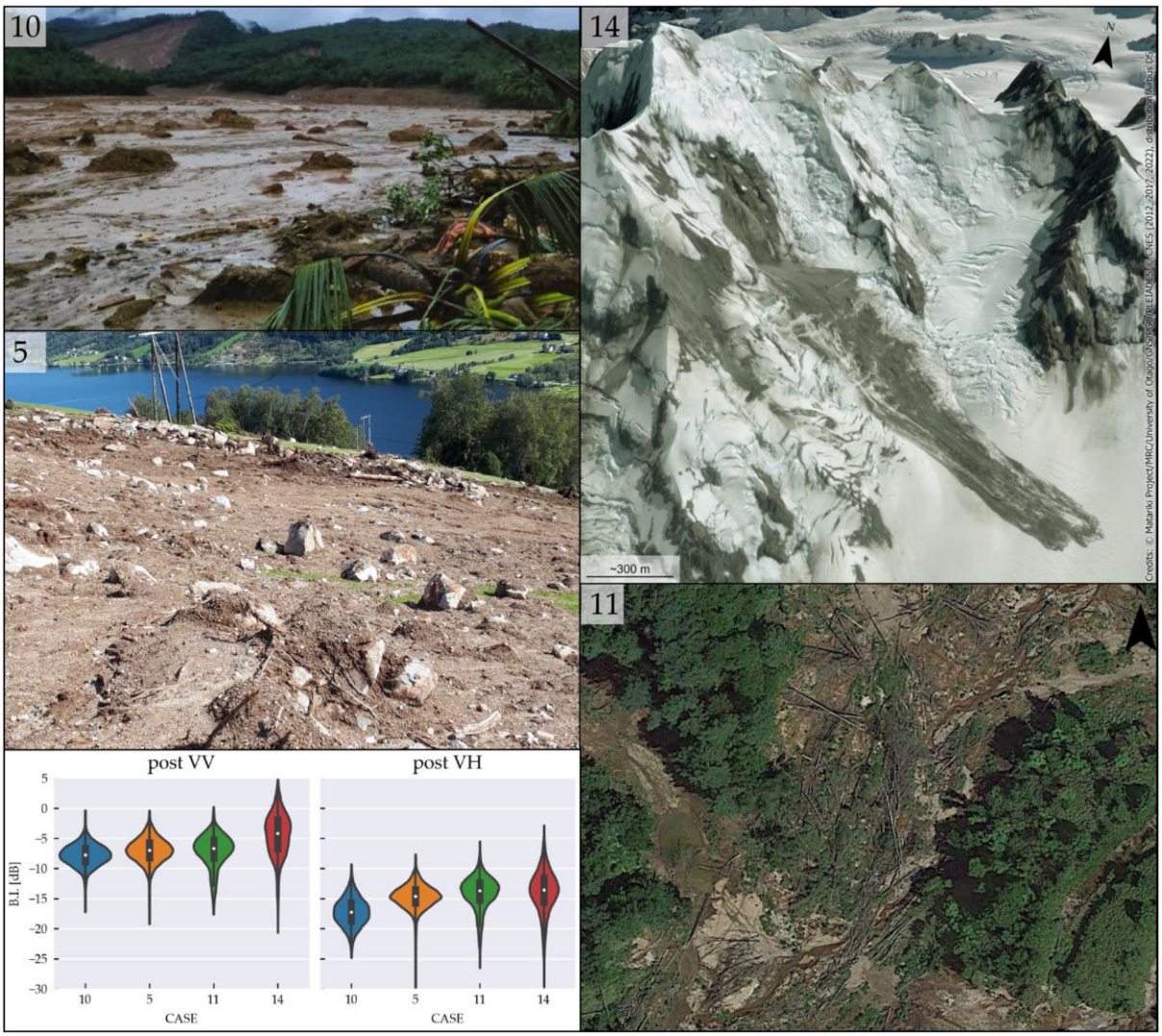

Figure 11 Different deposit material types, and the distribution of the pixel values from the four different case studies shown. These include: Smooth, flat deposits from mudflow near Baybay City, Philippines (10) (source: Philippines Coast Guard, AP). A mixture of soil and rocks in debris flow deposit in Vassenden, Norway (5). Rock avalanche deposits at Mt Tasman, New Zealand (14) (© Matariki Project/MRC/University of Otago/GNS/PGO/PLEIADES © CNES (2022), distribution Airbus DS.). (11) Forest debris from landslides in Hokkaido, Japan (© Maxar (2018)). Bottom left: Violin plots of post-event backscatter intensity distribution from the different deposit material types. The upper and lower quartiles and the median are indicated by the black box plot with a central white dot.

Preprints (www.preprints.org) | NOT PEER-REVIEWED | Posted: 22 February 2023 doi:10.20944/preprints202302.0390.v1

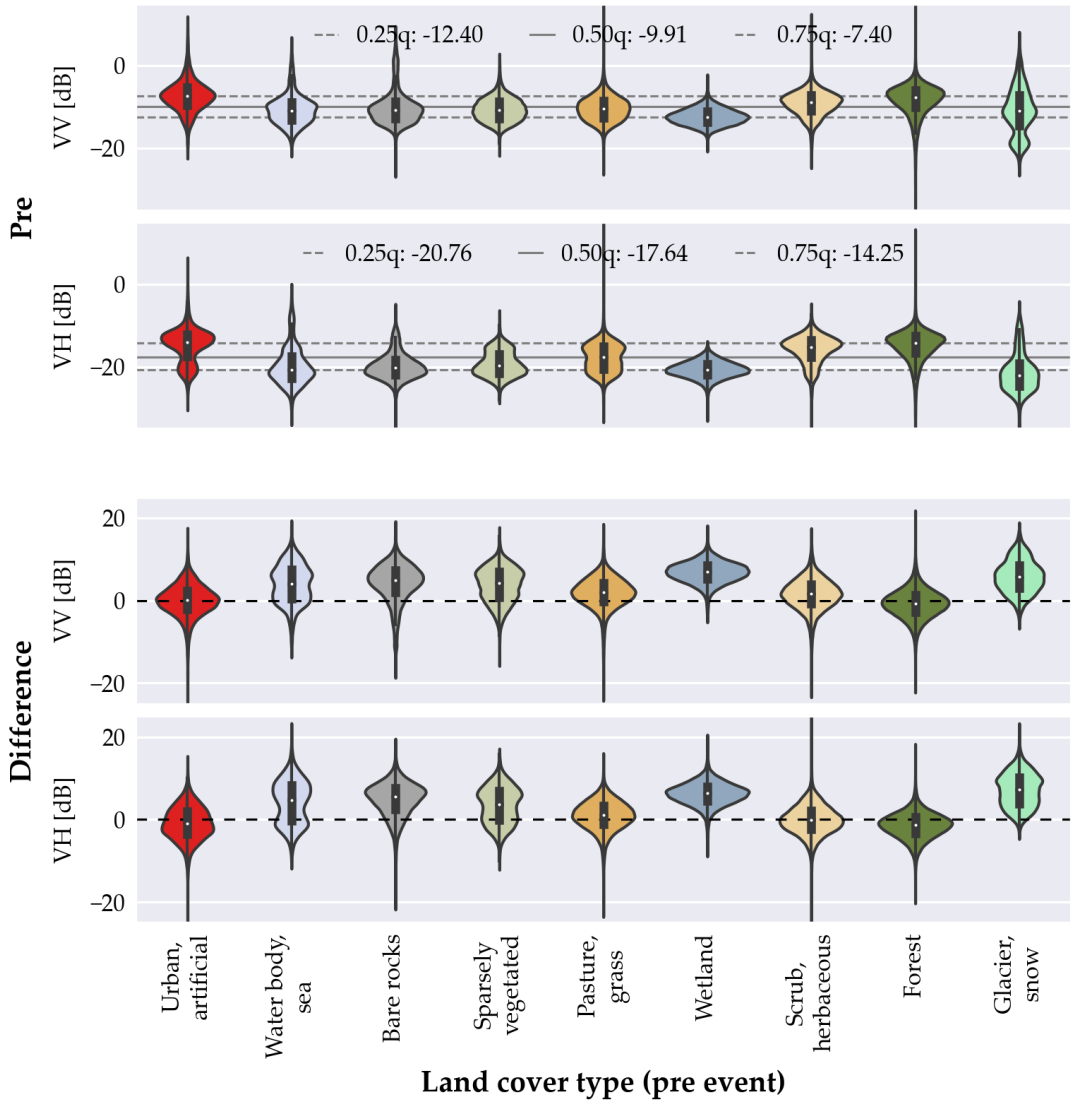

Figure 12 Distribution of sampled pixel values within mapped landslides from the pre-event and difference images, shown as violin plots with box-plots and kernel distribution. The upper and lower quartiles and the median are indicated by the black box plot with a central white dot. These are separated according to pre-event land cover types and polarisation.

Figure 12 shows the distribution of pixel values within the mapped landslide polygons according to land cover class, for pre-event and the change in backscatter intensity. The pre-event backscatter intensity values have a combined median of -9.9 and -17.6 dB for VV and VH respectively. Urban and forest land cover classes have slightly higher initial values relative to the median in VV and VH polarisations, while wetland and water bodies have slightly lower values in both. In VH non-vegetated land cover types including bare rocks and snow also show values lower than the median.

The differences in backscatter intensity are mostly positive, except for pixels within the forest class which show a mean decrease of -2 dB in both VV and VH polarisation. The strongest increases are observed for landslides that occurred in wetland and snow with average difference values of ~4 dB. Slightly negative changes are also seen for scrub and urban land cover classes in VH polarisation.

5.2.4 Seasonal variations and water content

Preprints (www.preprints.org) | NOT PEER-REVIEWED | Posted: 22 February 2023 doi:10.20944/preprints202302.0390.v1

The time-series plots in Figure 7 show variation in the seasonal cycles of backscatter intensity, in which reflect the local climate and vegetation conditions. In general, for vegetated areas the backscatter intensity is higher in summer, and lower in winter. While in tropical areas, the backscatter intensity is relatively constant through the year, and in sub-polar or alpine regions winter snowfalls produce strong decreases (in the order of 10 to 20 dB) in intensity. In most cases, the change due to landslides appears unambiguously and a clear difference in the seasonal cycle is observable. However, in cases with seasonal snow cover (e.g. 5B. Norway, 1B. Iceland and 14D. New Zealand) the changes due to landslides are of a lower magnitude than the change due to snow cover change, and therefore less clear.

Most of the inter-annual variability in the pre- and post-event seasonal cycles is likely caused by fluctuations in moisture content. Although we don't not have access to soil moisture measurements, some trends can be inferred. The effect of moisture content is seen most clearly in case 14 from a high alpine environment in New Zealand (Mt Tasman, approx. 2,500 m a.s.l.). Here, in spring at the onset of snow-melt, the backscatter intensity drops abruptly, with a magnitude of approximately 15 dB. In several cases, in the transit and deposit zones, it is seen that the following the initial change in backscatter intensity, there is a period over several weeks where the backscatter intensity decreases slightly. This is seen in cases 4, 2, and 5 in the herbaceous transit zone, and in 23 in the forested transit zone. We did not have access to soil moisture data, but it is possible that this pattern is due to decreasing moisture content after the rainfall triggered landslides. In contrast, the values increase in the deposit zone in case 15 in Iceland.

6. Discussion

The results showed that landslides produce predictable patterns in SAR backscatter change images related to morphology, land cover, and sensor and ground surface orientation. The trends identified have not previously been documented in relation to landslides. Here, we consider the physical basis for the identified trends in relation to the change in scattering mechanism, compare these with similar trends described in literature from other phenomena, and discuss limitations of the approach and possible future research directions.

6.1 Trends

In order to improve understanding of the physical-basis for the identified trends, we present the generalised conceptual model shown in Figure 13, relating the change in scattering behaviors to the observed change in backscatter intensity. This is described as follows, referring to the numbers illustrated:

Preprints (www.preprints.org) | NOT PEER-REVIEWED | Posted: 22 February 2023 doi:10.20944/preprints202302.0390.v1

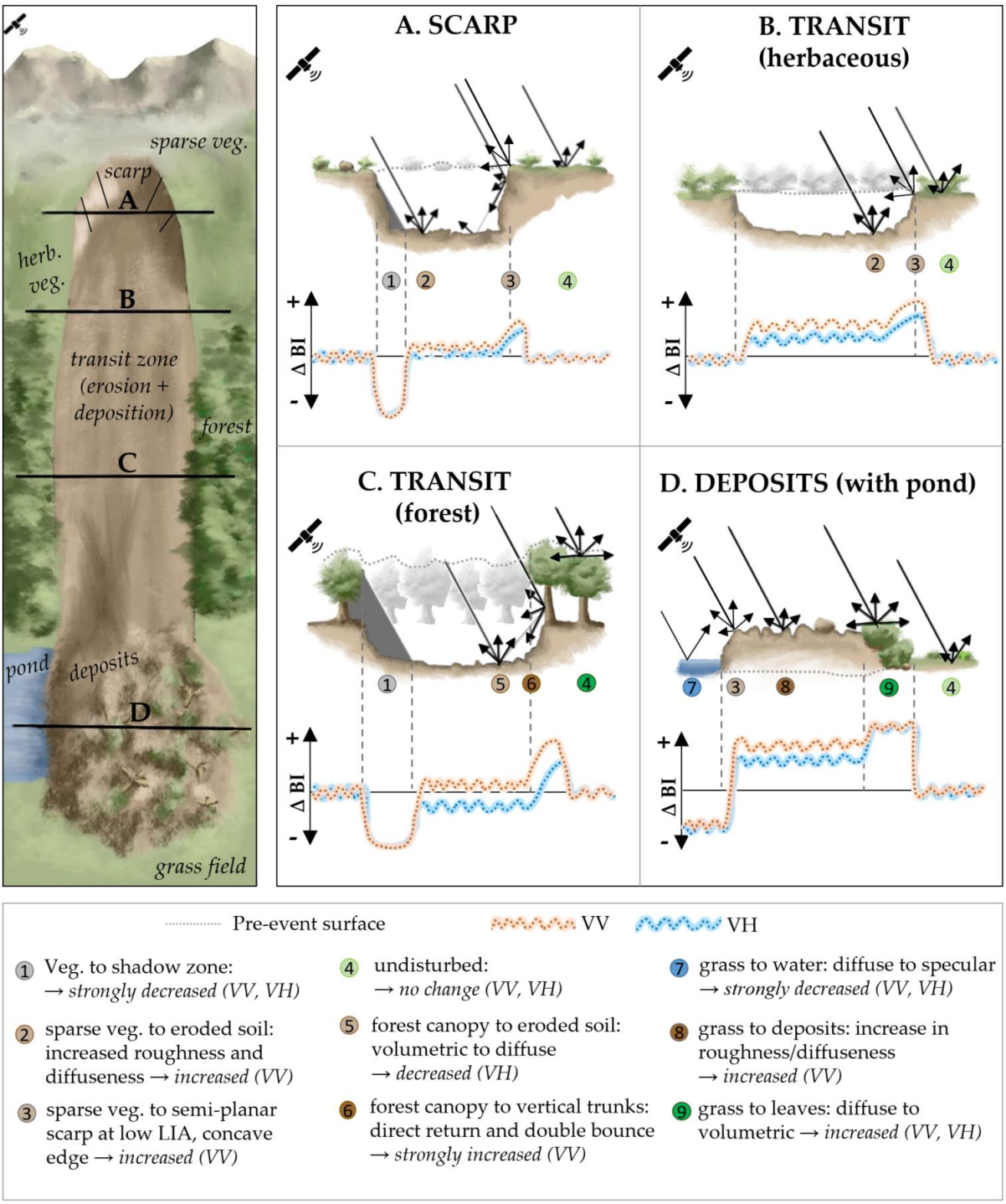

Figure 13 Conceptual model of a landslide and the relative changes in backscatter intensity (B.I.), depending on landslide morphology, and the change in ground-cover types and their associated scattering mechanisms.

A. SCARP

The sudden change in topography, usually expressed by a steep surface, results in a strongly decreased intensity for scarps facing away from the sensor (1). This is attributed to radar shadow, which occurs when the slope angle is steeper than the radar incident angle. The base of the scarp beyond the shadow zone, may show increased intensity due to an increase in surface roughness (2) as in the conceptual model. However, this will vary depending on the specific pre-event land cover and post-event surface

Preprints (www.preprints.org) | NOT PEER-REVIEWED | Posted: 22 February 2023 doi:10.20944/preprints202302.0390.v1

roughness and orientation. For scarps facing towards the sensor (3), if the LIA is decreased more energy will be reflected back towards the sensor, resulting in increased intensity. In addition, the concave top edge of the scarp will also give strongly increased reflectivity relative to a flat pre-event surface, producing strongly increased values on the outer edge of the scarp. These patterns are seen most clearly in VV, due to the greater sensitivity to changes in surface roughness. Similar changes have been documented in relation to changes in topography of a volcanic crater following an explosive eruption (Arnold et al., 2018).

B. TRANSIT (herbaceous)

The trend of predominantly increased backscatter intensity in these areas, is due to an increase in surface roughness of the landslide surface compared to a weathered pre-event surface (2). This results in increased diffusivity, and stronger reflection back towards the sensor. Minor scarps and concave features within transit zones of larger landslide are identifiable based on the same principles as described for the main scarp. There are numerous examples of agricultural studies relating increasing roughness of non-vegetated surfaces to increasing backscatter intensity (Baghdadi et al., 2018; Beaudoin et al., 1990)(Baghdadi et al., 2018; Beaudoin et al., 1990; Tempfli et al., 2009).

C. TRANSIT (forested)

The pattern illustrated for landslide transit zones in forest is very similar to the pattern described by (Hoekman et al., 2020) from drainage canals that are constructed within rainforests prior to deforestation. The changes relate to (1) radar shadow on the near edge, (5) change from forest to bare soil which produces a decrease in VH due to reduction of volumetric scattering, and possibly slight increase in VV, depending on the roughness of the surface, and (6) increased backscatter intensity on the far edge, due to a change from forest to a new near-vertical surface of the scarp and tree-trunks, which produce direct and double bounce scattering, increasing the energy returned to the sensor.

D. DEPOSITS (with ponding)

The example illustrated shows firstly a strong decrease caused by a new pond, related to a change from grass to water (7) which has a very low intensity due to specular reflection. From the case studies, we observed that new lakes or ponds caused by landslide dams, showed stronger signals than the landslides themselves and are very easy to detect in the change imagery. Although, they can be difficult to distinguish from scarps without contextual information, as can be seen in the Ecuador case, where there first seemed to be three large scarps, however one of them was actually a lake. Detecting newly formed lakes is important in disaster response, as these may occur in unpopulated areas, however can pose serious threats to people downstream if the landslide-dam bursts suddenly (Dellow et al., 2017). The signal is the same as can be used to detect flooding (Shen et al., 2019). Conversely, changes from ground to water result in strongly increased backscatter intensity which was observable in cases 10, 15 and 20 from the Philippines, Iceland and Peru.

The landslide deposits themselves were most frequently observed in change images by increased backscatter intensity (8) as is illustrated in the conceptual mode. This is due to increased surface roughness, and possibly also the presence of concave structures for landslides with a large volume, both of which produce increased diffusivity. However, as shown in Figure 6, 7 and 10, cases that

 doi:10.20944/preprints202302.0390.v1

appeared to have smooth deposits formed by fine materials (mud or silt) produce lower backscatter intensity post-event, and this may result in decreased backscatter intensity in VH change images. Such deposits can indicate that the sediments were deposited by still or slow-moving water, related to blocked drainage.

6.2 Controlling factors

Factors that were expected to control the visibility and expression of landslides in backscatter intensity change images included; geometric distortions, LIA, ground cover, seasonal variations and water content. Wavelength is also considered relevant, however was not investigated in this study. Overall, we saw significantly stronger trends in the time-series data from individual cases, than from the means of the pixels within the mapped polygons. This is due to the selection of points within the change images for extracting the time-series data that showed strong changes. While, the sample pixel values within the mapped polygons show more variation due to irregular surface texture and topography and speckle noise.

The overall detection rate was 87% (n. test cases = 26/30) in this study. This is similar to that reported by Mondini et. al (2019) of 83% (n. test cases = 27/32), yet differs significantly from the rate reported by Lindsay et al., (2022) of less than 10% (n. test cases = 9/120). The difference between these reported rates lies in the method of case study selection. In the two former, the examples selected came mostly from news reports and are biased towards larger, more catastrophic events, whereas in Lindsay et. al., (2022), the reported rate was in comparison to a set of previously mapped landslides from a single case study and included mainly smaller landslides.

The influence of the LIA was clearly observable when looking at the differences in the landslide expression between individual cases. This was particularly important in the case where landslides produced an abrupt change in surface height, whether due to removal of materials in the scarp area, or removal of trees in the transit or deposition zones. The pattern of shadows from steep or vertical surfaces facing away from the sensor, and bright edges facing towards the sensor is highly dependent on the sensor look direction (ascending or descending orbit path). The trends were not clear in the 2D histogram plots in this study, however the LIA has been shown to affect the backscatter intensity to different degrees, in experimental data from other fields where the sampled areas were more homogenous. Using post-event DEMs to estimate the LIA, would probably give clearer trends especially for the scarp. However, this data is not readily available in most cases (Dabiri et al., 2020).

The change in the ground cover type and associated scattering mechanisms was very important in determining the expression of the landslides. In the change images, time-series data, and statistical analyses, it was clear that landslides in forest tend to produce an overall decrease in backscatter intensity, while those in herbaceous and non-vegetated areas tend to produce an increase. In addition, changes to water bodies were very clear in the change images. Differences in the post-event backscatter intensity sampled within deposit zones, were also observed depending on the material size (fine, or coarse).

Changes due to landslides in time-series data were clearer for cases with tropical and temperate climates where the vegetation showed limited seasonal variation. Cases with changes in snow cover showed abrupt changes in backscatter intensity values that were not related to landslides. It was observable that the timing of landslides in relation to the underlying seasonal cycle, either enhanced

 doi:10.20944/preprints202302.0390.v1

(i.e. 14. New Zealand), or reduced (i.e. 5. Norway) the change in backscatter intensity. These variations in seasonal conditions are important to be aware of if designing an operational landslide detection system based on time-series data. The effect of changes in water content were not clear.

6.3 Limitations and future research directions

The cases that were undetectable in this study (Table 1, set 1) included two rock fall events, one slush flow, and one case with mixed vegetation type. In the rock fall events, it was determined that the change to the ground surface texture was not significant, or in the case where deposition occurred on a road, not permanent. The slush flow was not detectable due to changes to the surrounding area due to snow-melt. While for the mixed vegetation case where deposition occurred without removing the pre-existing trees, the change produced by the landslide did not significantly alter the backscatter response, which included both diffuse and volumetric scatterers, before and after the event. In the cases where landslides were only partially visible or detectable only with a-priori knowledge (set 2), the main limiting factors included; small or narrow landslide geometry, geometric distortions that obscured or warped the landslide signatures, snow- melt in the surrounding area, deposition in an urban area, and only single orbit pass available. Large scale topography, in particular high mountains, was not as problematic as expected.

The dataset produced in this study provides a diverse training dataset that can be used for developing generalised automatic detection models. Previous studies have shown that locally-trained deep-learning models such as U-Net can detect landslides with good accuracy from Sentinel-1 images due to their ability to differentiate random speckle noise from clusters of pixels related to changes to the ground surface (Ganerød et al., 2023). The results of this study can be used to improve the design of deep-learning models through understanding how to ensure representative training cases and relevant input data are included. A challenge for such models, will be to differentiate signals of non-landslide related vegetation loss from landslides, as is an ongoing problem for landslide detection using optical data (Prakash et al., 2021). More investigations could also be done using this dataset for improving understanding of how land cover affects the generation of post-event DEMs (Dabiri et al., 2020). Then automated estimation of the volume of material would also be possible. This would enable disaster responders to estimate the magnitude of the problem, and send appropriate resources.

Experience from testing these methods on recent events, including landslides triggered by floods and cyclones in New Zealand (10 January 2023, 27 January 2023), and the Turkey earthquakes (6 February 2023), has shown that large landslides and landslide dams can be detected from single post-event images. However. the greatest limitation for applying these methods in disaster situations is the lack of daily images freely available (revisit frequency in Europe is 1-3 days, in equatorial regions it can be up to 12 days). Commercial high resolution SAR data is currently available at a daily frequency. In order to be prepared to respond quickly, one should have agreements set up in advance to access to satellite images from as many sources as possible, including commercial providers (e.g. ALOS, ICEYE, Spacety which may provide data for research and non-commercial activities), and have code prepared to quickly process the images. Research should be conducted into combining imagery from multiple sensors with varying wavelengths, view angles and resolutions, to be prepared to use whatever information is available.

The frequency of freely available SAR images will double with the launch of the NISAR (NASA-ISRO SAR) satellites in 2024. However, it will take some time to build up a new set of landslides observations in the X- and L-band. Furthermore, it is likely that Sentinel-1 coherence data will be added to the GEE catalogue (Gorelick. N. (2022). *pers comm.*). This will facilitate global studies of how coherence data and backscatter data can be used together to improve landslide detection. Automatic detection and consequence analyses (for instance highlighting the intersection of automatically detected landslides with buildings, or infrastructure) could also be useful for improving situational awareness during disaster response.

7. Conclusions

When cloud-cover inhibits the use of optical imagery during disaster response, SAR satellite imagery could be used to provide crucial information on the location, and timing of landslides. Through systematic and quantitative analysis of over 1000 landslides from 30 diverse global case studies, we found that landslides produce predictable patterns of increased and decreased backscatter intensity. The change in intensity relates to morphology, and changes in topography, land cover, and surface roughness and their associated scattering properties. The findings were summarised in a physically, and empirically based conceptual model which can facilitate interpretation of landslides in SAR backscatter change images. These patterns have not been documented in relation to landslides previously, however have similarities to signals produced by features related to volcanic eruptions, agriculture, deforestation, canal building and floods. Using freely available Sentinel-1 images and Google Earth Engine, the radar change images can be rapidly produced for a new location, when new satellite images become available online. The trends observed in this study may improve utilisation of satellite radar images for rapid detection of landslides and other natural hazards, and facilitate development of multi-sensor automatic detection models and continuous monitoring systems. This can improve situational awareness in disaster response and potentially improve outcomes for the affected populations.

Data availability: The codes and dataset will be made available when published.

Description of author's responsibilities: Erin Lindsay performed the following roles: conceptualisation, data curation, formal analysis, investigation, methodology, software, validation, visualisation, writing – original draft, and writing – review & editing. Graziella Devoli contributed with the roles: visualisation, review & editing and supervision. Johannes Reiche performed review & editing, and methodology. Steinar Nordal performed review & editing, supervision, and funding acquisition. Regula Frauenfelder contributed with methodology, review & editing and visualization. Alexandra Jarna performed data curation, investigation and visualisation. Lars-Christian Tokle assisted with, methodology, software, validation and visualisation.

Funding: This research was funded by the Research Council of Norway, through the research project *SFI Klima 2050* [grant number 237859].

Acknowledgements: Data provided by the European Space Agency and Planet under project ID: 192991 - *Optical satellite data for landslide detection using dNDVI method.* Project supported by ESA Network of Resources Initiative. The authors gratefully acknowledge the time, materials, and efforts contributed by the following people: Jørn Emil Gaarder (Klima 2050, NTNU) for illustrations, Angel Valdiviezo A. (Escuela Superior Politécnica del Litoral), Oddur Sigurdson and Tómas Jóhannesson (Icelandic Meteorological Office), Kevin Dockery (former Irish Garda), Sigurd Nerhus and Denise Ruther

 doi:10.20944/preprints202302.0390.v1

(Western Norway University of Applied Sciences), Gylfi Gylfason (Just Icelandic), Bo Liu (Southwest Jiaotong University), Margaret Darrow (University of Alaska Fairbanks), Pascal Sirguey (Mountain Research Centre, Aotearoa/New Zealand) for kindly providing photos. Kejie Chen (Southern University of Science and Technology), for discussions of case study #13. Corey Scheip (BGC) for recommending case studies. Forrest Williams (Alaska Space Facility) and Eirik Malnes (NORCE) for discussing the interpretation of edges. Al Handwerger (JPL Laboratory, NASA), for feedback on SAR image processing method. Erlend Andenaes, Ivan Depina, Ola Fredin, and Tore Kvande (NTNU) for discussion of results and support.

Appendix 1: Links for landslide case study reports Accessed: 11-Dec-2022.

Location	Link
1. Iceland	https://blogs.agu.org/landslideblog/2021/10/08/multiple-landslides-in-thingeyjarsveit-and-in-kinnarfjoll-in-iceland/
2. Ireland	https://blogs.agu.org/landslideblog/2021/07/23/benbrack-1/
3. New Zealand	https://blogs.agu.org/landslideblog/2022/04/21/wairoa-1-2/
4. Ecuador	https://blogs.agu.org/landslideblog/2021/02/16/chunchi-a/
5. Norway	https://blogs.agu.org/landslideblog/2019/08/01/sogn-og-fjordane-1/
6. Sth. Africa	https://blogs.agu.org/landslideblog/2022/04/22/durban-1/
7. Vanuatu	https://hazmapper.org/2020/05/20/cyclone-harold-defoliation-and-mass-wasting-in-vanuatu/
8. Brazil	https://blogs.agu.org/landslideblog/2021/05/17/the-17-18-december-2020-landslide-disaster-in-presidente-getulio-southern-brazil/
9. China	https://blogs.agu.org/landslideblog/2021/10/28/the-21-july-2020-shaziba-landslide-at-mazhe-village-in-enshi-china/
10. Philippines	https://blogs.agu.org/landslideblog/2022/04/14/three-very-large-landslides-triggered-by-tropical-storm-megi-agaton/
11. Japan	https://link.springer.com/article/10.1007/s10346-019-01206-7
12. USA	https://blogs.agu.org/landslideblog/2022/08/03/haines/
13. China	https://blogs.agu.org/landslideblog/2021/10/26/the-5-april-2021-tiejiangwan-landslide-in-sichuan-province-china/
14. N. Zealand	https://www.otago.ac.nz/surveying/potree/pub/mrc/projects/matariki/changing-landscape
15. Iceland	https://blogs.agu.org/landslideblog/2018/07/26/fagraskogarfjall-landslide/
16. India	https://link.springer.com/article/10.1007/s10346-021-01802-6
17. India	https://link.springer.com/article/10.1007/s10346-021-01802-6
18. Norway	https://www.regobs.no/Registration/193067
19. India	https://link.springer.com/article/10.1007/s10346-020-01598-x
20. Peru	https://blogs.agu.org/landslideblog/2020/06/30/achoma-landslide-1/
21. Kygysztan	https://earthobservatory.nasa.gov/images/90255/landslide-in-southern-kyrgyzstan
22. Italy	https://blogs.agu.org/landslideblog/2019/11/25/savona-landslide-1/
23. Indonesia	https://blogs.agu.org/landslideblog/2022/03/29/mount-talakmau-1/
24. Brazil	https://blogs.agu.org/landslideblog/2022/05/31/recife-1/
25. Canada	https://blogs.agu.org/landslideblog/2021/11/16/bc-1/
26. USA	https://twitter.com/bclemms/status/1452333926949822468?lang=en
27. Burundi	https://hazmapper.org/2020/04/27/mass-wasting-in-burundi-december-2019/
28. Australia	https://blogs.agu.org/landslideblog/2022/03/11/main-arm-1/
29. Indonesia	https://link.springer.com/article/10.1007/s10346-021-01700-x
30. Turkey	https://blogs.agu.org/landslideblog/2019/05/17/ordu-1/

References:

Arnold, D.W.D., Biggs, J., Wadge, G., Mothes, P., 2018. Using satellite radar amplitude imaging for monitoring syn-eruptive changes in surface morphology at an ice-capped stratovolcano. Remote Sens. Environ. 209, 480–488. https://doi.org/https://doi.org/10.1016/j.rse.2018.02.040

ASF, 2022. Introduction to SAR [WWW Document]. ASF HyP3 User Guid. URL https://hyp3-docs.asf.alaska.edu/guides/introduction_to_sar/ (accessed 10.27.22).

Baghdadi, N., El Hajj, M., Choker, M., Zribi, M., Bazzi, H., Vaudour, E., Gilliot, J.-M., Ebengo, D.M., 2018. Potential of Sentinel-1 Images for Estimating the Soil Roughness over Bare Agricultural Soils. Water 10. https://doi.org/10.3390/w10020131

Ban, Y., Zhang, P., Nascetti, A., Bevington, A.R., Wulder, M.A., 2020. Near real-time wildfire progression monitoring with Sentinel-1 SAR time series and deep learning. Sci. Rep. 10, 1–15.

Beaudoin, A., Le Toan, T., Gwyn, Q.H.J., 1990. SAR observations and modeling of the C-band backscatter variability due to multiscale geometry and soil moisture. IEEE Trans. Geosci. Remote Sens. 28, 886–895. https://doi.org/10.1109/36.58978

Bouvet, A., Mermoz, S., Ballère, M., Koleck, T., Le Toan, T., 2018. Use of the SAR Shadowing Effect for Deforestation Detection with Sentinel-1 Time Series. Remote Sens. 10. https://doi.org/10.3390/rs10081250

Breiman, L., Friedman, J.H., Olshen, R.A., Stone, C.J., 2017. Classification and regression trees. Routledge.

Burrows, K., Marc, O., Remy, D., 2022. Using Sentinel-1 radar amplitude time series to constrain the timings of individual landslides: a step towards understanding the controls on monsoon-triggered landsliding. Nat. Hazards Earth Syst. Sci. 22, 2637–2653.

Casagli, N., Guzzetti, F., Jaboyedoff, M., Nadim, F., Petley, D.N., 2017. Hydrological risk: landslides. Underst. Disaster Risk Hazard Relat. Risk Issues-section II 209–218.

Chorlton, L.B., 2007. Generalized geology of the world: bedrock domains and major faults in GIS format (WMS). Geol. Surv. Canada, Open File 5529.

Cigna, F., Bateson, L.B., Jordan, C.J., Dashwood, C., 2014. Simulating SAR geometric distortions and predicting Persistent Scatterer densities for ERS-1/2 and ENVISAT C-band SAR and InSAR applications: Nationwide feasibility assessment to monitor the landmass of Great Britain with SAR imagery. Remote Sens. Environ. 152, 441–466. https://doi.org/https://doi.org/10.1016/j.rse.2014.06.025

Copernicus, 2019. Copernicus Global Land Cover Layers: CGLS-LC100 Collection 3 [WWW Document]. Earth Engine Dev. URL https://developers.google.com/earth-engine/datasets/catalog/COPERNICUS_Landcover_100m_Proba-V-C3_Global?hl=en

Dabiri, Z., Hölbling, D., Abad, L., Helgason, J.K., Sæmundsson, Þ., Tiede, D., 2020. Assessment of Landslide-Induced Geomorphological Changes in Hítardalur Valley, Iceland, Using Sentinel-1 and Sentinel-2 Data. Appl. Sci. 10. https://doi.org/10.3390/app10175848

Dave Petley, 2022. The Landslide Blog [WWW Document]. URL https://blogs.agu.org/landslideblog

Dellow, S., Massey, C., Cox, S., 2017. Response and initial risk management of landslide dams caused by the 14 November 2016 Kaikoura earthquake, South Island, New Zealand, in: Proceedings of the 20th NZGS Geotechnical Symposium, Napier, New Zealand.

EEA/Copernicus, 2012. Copernicus CORINE Land Cover [WWW Document]. Earth Engine Dev. URL https://developers.google.com/earth-engine/datasets/catalog/COPERNICUS_CORINE_V20_100m

Froude, M.J., Petley, D.N., 2018. Global fatal landslide occurrence from 2004 to 2016. Nat. Hazards Earth Syst. Sci. 18, 2161–2181. https://doi.org/10.5194/nhess-18-2161-2018

Fung, A.K., Li, Z., Chen, K.-S., 1992. Backscattering from a randomly rough dielectric surface. IEEE Trans. Geosci. Remote Sens. 30, 356–369.

Ganerød, A.J., Lindsay, E., Fredin, O., Myrvoll, T.-A., Nordal, S., Rød, J.K., 2023. Globally-vs Locally-trained Machine Learning Models for Land-slide Detection: A Case Study of a Glacial Landscape.

Gariano, S.L., Guzzetti, F., 2016. Landslides in a changing climate. Earth-Science Rev. https://doi.org/10.1016/j.earscirev.2016.08.011

GFDRR, 2023. Global Landslide Hazard Map [WWW Document]. World Bank. URL https://datacatalog.worldbank.org/search/dataset/0037584

Ghorbanzadeh, O., Blaschke, T., Gholamnia, K., Meena, S.R., Tiede, D., Aryal, J., 2019. Evaluation of Different Machine Learning Methods and Deep-Learning Convolutional Neural Networks for Landslide Detection. Remote Sens. 11. https://doi.org/10.3390/rs11020196

Gorelick, N., Hancher, M., Dixon, M., Ilyushchenko, S., Thau, D., Moore, R., 2017. Google Earth Engine: Planetary-scale geospatial analysis for everyone. Remote Sens. Environ. 202, 18–27.

Guzzetti, F., Mondini, A.C., Cardinali, M., Fiorucci, F., Santangelo, M., Chang, K.-T., 2012. Landslide inventory maps: New tools for an old problem. Earth-Science Rev. 112, 42–66. https://doi.org/10.1016/J.EARSCIREV.2012.02.001

Handwerger, A.L., Huang, M.-H., Jones, S.Y., Amatya, P., Kerner, H.R., Kirschbaum, D.B., 2022. Generating landslide density heatmaps for rapid detection using open-access satellite radar data in Google Earth Engine. Nat. Hazards Earth Syst. Sci. 22, 753–773.

Hanssen-Bauer, I., Drange, H., Førland, E.J., Roald, L.A., Børsheim, K.Y., Hisdal, H., Lawrence, D., Nesje, A., Sandven, S., Sorteberg, A., others, 2009. Climate in Norway 2100. Backgr. Inf. to NOU Clim. Adapt. (In Nor. Klima i Norge 2100. Bakgrunnsmateriale til NOU Klim. Oslo Nor. klimasenter.

Hijmans, R.J., Cameron, S.E., Parra, J.L., Jones, P.G., Jarvis, A., 2005. Very high resolution interpolated climate surfaces for global land areas. Int. J. Climatol. A J. R. Meteorol. Soc. 25, 1965–1978. https://doi.org/10.1002/joc.1276.

Hoekman, D., Kooij, B., Quiñones, M., Vellekoop, S., Carolita, I., Budhiman, S., Arief, R., Roswintiarti, O., 2020. Wide-Area Near-Real-Time Monitoring of Tropical Forest Degradation and Deforestation Using Sentinel-1. Remote Sens. 12. https://doi.org/10.3390/rs12193263

Hungr, O., Leroueil, S., Picarelli, L., 2014. The Varnes classification of landslide types, an update. Landslides 11, 167–194. https://doi.org/10.1007/s10346-013-0436-y

Katiyar, V., Tamkuan, N., Nagai, M., 2021. Near-real-time flood mapping using off-the-shelf models with SAR imagery and deep learning. Remote Sens. 13, 2334.

Kedia, T., Ratcliff, J., O'Connor, M., Oluic, S., Rose, M., Freeman, J., Rainwater-Lovett, K., 2022. Technologies Enabling Situational Awareness During Disaster Response: A Systematic Review. Disaster Med. Public Health Prep. 16, 341–359. https://doi.org/10.1017/dmp.2020.196

Kellndorfer, J., Flores-Anderson, A.I., Herndon, K.E., Thapa, R.B., 2019. Using SAR data for mapping deforestation and forest degradation. SAR Handbook. Compr. Methodol. For. Monit. Biomass Estim. ServirGlobal Hunstville, AL, USA 65–79.

Kjekstad, O., Highland, L., 2009. Economic and Social Impacts of Landslides, in: Landslides – Disaster Risk Reduction. Springer Berlin Heidelberg, Berlin, Heidelberg, pp. 573–587. https://doi.org/10.1007/978-3-540-69970-5_30

Kottek, M., Grieser, J., Beck, C., Rudolf, B., Rubel, F., 2006. World map of the Köppen-Geiger climate classification updated.

Lacroix, P., Bièvre, G., Pathier, E., Kniess, U., Jongmans, D., 2018. Use of Sentinel-2 images for the detection of precursory motions before landslide failures. Remote Sens. Environ. 215, 507–516.

Lindsay, E., Frauenfelder, R., Rüther, D., Nava, L., Rubensdotter, L., Strout, J., Nordal, S., 2022. Multi-Temporal Satellite Image Composites in Google Earth Engine for Improved Landslide Visibility: A Case Study of a Glacial Landscape. Remote Sens. 14. https://doi.org/10.3390/rs14102301

Meyer, F., 2019. Spaceborne Synthetic Aperture Radar: Principles, Data Access, and Basic Processing Techniques, in: SAR Handbook: Comprehensive Methodologies for Forest Monitoring and Biomass Estimation. NASA.

Mondini, A., Santangelo, M., Rocchetti, M., Rossetto, E., Manconi, A., Monserrat, O., 2019. Sentinel-1 SAR Amplitude Imagery for Rapid Landslide Detection. Remote Sens. 11, 760. https://doi.org/10.3390/rs11070760

Mondini, A.C., Guzzetti, F., Chang, K.-T., Monserrat, O., Martha, T.R., Manconi, A., 2021. Landslide failures detection and mapping using Synthetic Aperture Radar: Past, present and future. Earth-Science Rev. 216, 103574. https://doi.org/https://doi.org/10.1016/j.earscirev.2021.103574

Nava, L., Monserrat, O., Catani, F., 2022. Improving Landslide Detection on SAR Data Through Deep Learning. IEEE Geosci. Remote Sens. Lett. 19, 1–5. https://doi.org/10.1109/LGRS.2021.3127073

Prakash, N., Manconi, A., Loew, S., 2021. A new strategy to map landslides with a generalized convolutional neural network. Sci. Rep. 11, 9722. https://doi.org/10.1038/s41598-021-89015-8

Reiche, J., Mullissa, A., Slagter, B., Gou, Y., Tsendbazar, N.-E., Odongo-Braun, C., Vollrath, A., Weisse, M.J., Stolle, F., Pickens, A., others, 2021. Forest disturbance alerts for the Congo Basin using Sentinel-1. Environ. Res. Lett. 16, 24005.

Santangelo, M., Cardinali, M., Bucci, F., Fiorucci, F., Mondini, A.C., 2022. Exploring event landslide mapping using Sentinel-1 SAR backscatter products. Geomorphology 397, 108021. https://doi.org/https://doi.org/10.1016/j.geomorph.2021.108021

Shen, X., Wang, D., Mao, K., Anagnostou, E., Hong, Y., 2019. Inundation Extent Mapping by Synthetic Aperture Radar: A Review. Remote Sens. 11. https://doi.org/10.3390/rs11070879

 doi:10.20944/preprints202302.0390.v1

Sudmanns, M., Tiede, D., Augustin, H., Lang, S., 2020. Assessing global Sentinel-2 coverage dynamics and data availability for operational Earth observation (EO) applications using the EO-Compass. Int. J. Digit. Earth 13, 768–784.

Tempfli, K., Huurneman, Gc., Bakker, Wh., Janssen, L.L.F., Feringa, W.F., Gieske, A.S.M., Grabmaier, K.A., Hecker, C.A., Horn, J.A., Kerle, N., others, 2009. Principles of remote sensing: an introductory textbook. International Institute for Geo-Information Science and Earth Observation.

Ulaby, F., Dobson, M.C., Álvarez-Pérez, J.L., 2019. Handbook of radar scattering statistics for terrain. Artech House.

van Natijne, A.L., Bogaard, T.A., van Leijen, F.J., Hanssen, R.F., Lindenbergh, R.C., 2022. World-wide InSAR sensitivity index for landslide deformation tracking. Int. J. Appl. Earth Obs. Geoinf. 111, 102829. https://doi.org/https://doi.org/10.1016/j.jag.2022.102829

Vollrath, A., Mullissa, A., Reiche, J., 2020. Angular-Based Radiometric Slope Correction for Sentinel-1 on Google Earth Engine. Remote Sens. 12. https://doi.org/10.3390/rs12111867

Waksom, M., 2022a. seaborn.violinplot [WWW Document]. Seaborne. URL https://seaborn.pydata.org/generated/seaborn.violinplot.html?highlight=violin&fbclid=IwAR1DDTMdluEMZNbvKMfFiUO0jhRCyWcmYBCqvBUBPopybyNPHRTtGJIRIYI#seaborn.violinplot

Waksom, M., 2022b. seaborn.histplot [WWW Document]. Seaborne. URL https://seaborn.pydata.org/generated/seaborn.histplot.html?highlight=histplot&fbclid=IwAR3jDVV1F0iX5S8ATZhxqnXhgAa22vMzFx3GkANQKFc1xYuicPVdQk9BmXM#seaborn.histplot

Williams, J.G., Rosser, N.J., Kincey, M.E., Benjamin, J., Oven, K.J., Densmore, A.L., Milledge, D.G., Robinson, T.R., Jordan, C.A., Dijkstra, T.A., 2018. Satellite-based emergency mapping using optical imagery: experience and reflections from the 2015 Nepal earthquakes. Nat. hazards earth Syst. Sci. 18, 185–205.

Zhang, P., Ban, Y., Nascetti, A., 2021. Learning U-Net without forgetting for near real-time wildfire monitoring by the fusion of SAR and optical time series. Remote Sens. Environ. 261, 112467.